EFFECT OF HIP/RPL29 ABSENCE ON ADULT BONE PROPERTIES IN MICE

by

Laura Sloofman

A thesis submitted to the Faculty of the University of Delaware in partial fulfillment of the requirements for the degree of Bachelor of Science in Quantitative Biology with Distinction.

Spring 2010

EFFECT OF HIP/RPL29 ABSENCE ON ADULT BONE PROPERTIES IN MICE

by

Laura Sloofman

Approved: _____

Catherine Kirn-Safran, Ph.D.
Professor in charge of thesis on behalf of the Advisory Committee

Approved: _____

Liyun Wang, Ph.D.
Committee member from the Department of Mechanical Engineering

Approved: _____

Gilberto Schleiniger, Ph.D.
Committee member from the Department of Mathematical Sciences

Approved: _____

Rolf Joerger, Ph.D.
Committee member from the Board of Senior Thesis Readers

Approved: _____

Ismat Shah, Ph.D.

Chair of the University Committee on Student and Faculty Honors

ACKNOWLEDGMENTS

First and foremost I would like to thank Dr. Catherine Kirn-Safran for taking me into her laboratory 3 years ago. Catherine, your dedication, confidence, tenacity and support has been invaluable. You have pushed me to become a better writer, observer and interpreter. I am honored to have been your student, and I am proud to call you my first mentor.

I would also like to thank the Kirn-Safran laboratory, especially Daniel Oristian who served as my graduate student mentor during my first year. Additionally I would like to thank everybody in the Carson and Farach-Carson laboratories. Your moral support has been invaluable. Also, thank you to Drs. Liyun Wang and John Novotny in the Department of Mechanical Engineering for your help with the mechanical testing. Thank you Dr Rolf Joerger for your valuable feedback, and for serving as my third reader.

To Drs. Gilberto Schleiniger, John A. Pelesko, and to all of my professors and friends in the Department of Mathematics, thank you for your unyielding support throughout my undergraduate career. Thank you for developing the Quantitative Biology degree program, with the help of Drs. David Usher and Harold White in Biology. Because of your efforts, this Bewick's Wren (or House Wren if I'm feeling especially competitive) is ready to fly.

Mom, Dad and Bonnie (the best sister ever), thank you for everything. I can't find the words to express how grateful I am to have come from this family. And since my nickname is chatterbox, that is quite a feat. I love you.

Finally I would like to thank whoever installed the round table near the third floor kitchenette in Wolf Hall. Your foresight and design planning gave me the perfect place to complete most of my homework, and this thesis.

TABLE OF CONTENTS

LIST OF TABLES

LIST OF FIGURES

LIST OF ABBREVIATIONS

AP	Anterior-posterior
BMC	Bone mineral content
BMD	Bone mineral density
DNA	Deoxyribonucleic acid
E	Elasticity
EI	Bending rigidity
ES	Embryonic stem
FTIR	Fourier-Transform Infrared
FTIRI	Fourier-Transform Infrared Imaging
HET	Heterozygous
HIP/RPL29	Heparin Sulfate Interacting Protein/Ribosomal Protein L29
Hp/HS	Heparin/heparin sulfate
I_{ML}	Medial-lateral moment of Inertia
micro-CT	Micro-computed tomography
ML	Medial-lateral
mRNA	Messenger RNA
PBS	Phosphate buffered saline
PYD	Post yield displacement
RNA	Ribonucleic acid
ROI	Region of interest
RPs	Ribosomal Proteins
TAE	Tris acetate ethylenediaminetetraacetic acid
TMD	Tissue mineral density

tRNA	Transfer RNA
WT	Wild type
XLR	Collagen crosslinking

ABSTRACT

Ribosomal proteins (RPs) play an important role in the maintenance of a normal protein synthetic rate. Our group generated the first viable mouse mutant model lacking an individual ribosomal protein, HIP/RPL29. Decreased rates of proliferation and protein synthesis in these mutants resulted in skeletal growth defects leading to short stature at birth, which persist during adulthood. We used HIP/RPL29 knockout mice to elucidate the role of this protein in bone structure and rigidity. We hypothesized that a decrease in protein biosynthesis affecting matrix production in HIP/RPL29 knockout mice lowers bone mass and increases bone fragility. Cortical bone microstructure of HIP/RPL29-deficient and wild type six-month-old femurs was assessed at the mid-shaft using micro-computed tomography (micro-CT). Significant differences in the bone composition were found between the HIP/RPL29-null and control mice. Interestingly, we observed a partial preservation of cortical thickness in male samples, coupled with significant increases in bone mineral content. This observation was only found in male samples, indicating a gender-specific effect of HIP/RPL29 deletion on cortical bone parameters. Additionally, null males, and females to a lesser extent, showed increased bone material toughness to compensate for their decreased size. Despite these gender-modulated differences, neither males nor females could withstand comparable forces under three-point bending tests. Moreover, smaller post-yield displacements (and therefore increased bone brittleness) were found in HIP/RPL29-null animals relative to controls.

To gain further insight behind the molecular changes induced by this mutation, we examined the Fourier transform infrared (FT-IR) spectroscopic profiles of one, three and six month old hard resin-embedded tibiae. Consistent with the six-

month microCT data, we found increased mineral-to-matrix ratios in the growth plate of male null mice, which were not observed in the female tibiae. FT-IR analysis showed that a significant decrease in the collagen crosslinking parameter during the maturation of HIP/RPL29-deficient bone precedes an overall enhancement in the relative extent of mineralization of cortical and trabecular bone. Interestingly, HIP/RPL29 knockout in teeth, another mineralized tissue, results in increases in both dentin and enamel mineral densities. This hypermineralization could be responsible for the brittle bone phenotype in HIP/RPL29-deficient samples. Due to machine limitations, we could not assess whether or not these limitations altered the anabolic response to mechanical loading in HIP/RPL29-deficient samples.

After the differences in structural, material and molecular composition in HIP/RPL29-deficient cortical bone were established, it became apparent that the altered geometry of HIP/RPL29 mice could influence bone microstructure due to loading discrepancies resulting from the short stature phenotype of HIP/RPL29 mice. Mathematical modeling using beam theory was used to determine the relative influence of bone geometry on stiffness calculations. We found that femoral stiffness at six months was best without directly accounting for the geometrical discrepancies of the mutant samples versus age and gender-matched controls.

Chapter 1

INTRODUCTION

1.1 Bone formation and remodeling

Bone is a dynamic tissue composed of two phases, an organic and inorganic phase. The organic phase is composed of type I collagen and various extracellular matrix components sequestering growth factors. Carbonated hydroxyapatite forms the inorganic phase (Robinson et al., 1953).

Bone forms during the fetal stage of development by intramembranous ossification and endochondral ossification, which occurs during the formation of the flat bones of the skull, while endochondral ossification occurs in long bones. In endochondral ossification bone is formed from pre-existing cartilage. Bone marrow, a non-mineralized source of stem cells, produces new blood cells in long bones. It is believed that osteocytes act as mechanosensing cells in bone that can monitor (detect) the mechanical strain in bone and can modulate both osteoclasts and osteoblasts during bone remodeling (Cowin et al., 1995). These cells are distributed throughout the bone matrix and their extensions form a network in the lacuna canalicular system in order to communicate with each other and between osteocytes and effector cells outside the matrix. It is believed that bone is removed by osteoclasts when a mechanical stimulus is not present and added by osteoblasts when a stimulus is detected. This cellular network participates in the maintenance of both the bone quantity and quality of cortical and trabecular bone (Martin et al., 2000).

1.2 Trabecular bone

Trabecular bone is found internally, near the ends of long bone. It is composed of small thin struts of calcified tissues (Hart et al., 1995). Trabecular bone helps absorb shock due to its spongy nature. It is softer, weaker and less dense than cortical bone. It has a complex structure consisting mostly of struts and plates (Ruimerman et al., 2005). Trabecular bone is a vascular tissue, frequently containing red bone marrow where the production of blood cells occurs. Trabecular bone is highlighted in Figure 1.

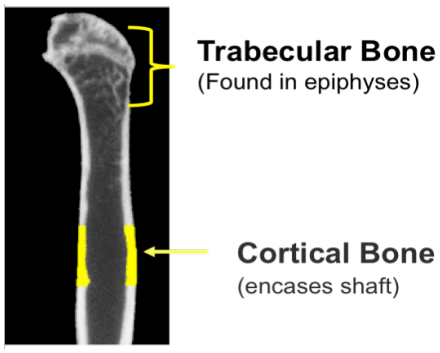

Figure 1: Basic schematic of long bone. Trabecular bone is found near the yellow bracket at the distal and proximal ends of long bone while cortical bone encases the shaft of long bones providing protection and stability to the tissue.

1.3 Cortical bone

Cortical bone, commonly known as the compact bone found in the shaft of long bones, is a dense tissue which is penetrated by blood vessels through a network of canaliculi (Ruimerman et al., 2005). Cortical bone is depicted in Figure 1 and corresponds to the hard casing around the bone marrow and is particularly visible at mid-shaft.

1.4 Function of Ribosomal Proteins

The ribosome is an integral part of the cell whose main function is translation, defined as transcribing the genetic code present on mRNA into functional proteins. Found in prokaryotes and eukaryotes, ribosomes are essential components of the cellular machinery. Generally proteins present in the ribosome are essential for proper growth and development of viable organisms.

The eukaryotic 80S ribosome is composed of two subunits, 60S and 40S. Both ribosomal subunits are composed of ribosomal RNA and ribosomal proteins. The small and large ribosomal subunits contain approximately 33 and 49 ribosomal proteins, respectively. Since each type of ribosomal protein has a different molecular structure, it is assumed that each protein class also serves a different function in the ribosome. Early studies using neuron-scattering and immunoelectroscopy indicated that ribosomal proteins are present on the surface of the ribosome (Capel et al., 1988 and Stoffler et al., 1984). Generally, ribosomal proteins aid in messenger RNA (mRNA) and transfer RNA (tRNA) recognition, and tRNA decoding. The core of the ribosome contains ribosomal RNA (rRNA). rRNA acts as the provider of the basic framework for the ribosome and is a necessary catalyst for the formation of peptide bonds (Brodersen and Nielson et al., 2005).

1.5 Heparin Sulfate Interacting Protein/Ribosomal Protein L 29 (HIP/RPL29)

One of these ribosomal proteins, Ribosomal Protein L29 (HIP/RPL29), is present in yeast at the interface between both subunits. It is believed to play a role in subunit assembly. This ribosomal protein is located on the large subunit. Murine HIP/RPL29, a highly basic ribosomal protein, is composed of 160 amino acids. Eukaryotic HIP/RPL29 has an apparent molecular weight of 28 kDa on SDS-PAGE (Oristian et al., 2007). The presence of many lysine residues results in the polycationic nature of this molecule. It has also been demonstrated that HIP/RPL29 selectively binds heparin/heparin sulfate (Hp/HS) chains of proteoglycans (Rohde et al., 1996).

HIP/RPL29 is 84% similar to the human ortholog. A strong conservation of the gene structure was also demonstrated (Hoke et al., 1998, Kirn-Safran et al., 2002). The NH_2-terminal portion of the protein is highly conserved across phyla such as Drosophila, yeast, and plants while the COOH-terminal region is absent in invertebrates and lower organisms. In contrast to the NH_2-terminal portion, the COOH-terminal region is believed to possess extra-ribosomal functions (Kirn-Safran et al., 2000)

1.6 Link between HIP/RPL29 and skeletogenesis

Since ribosomes aid in global protein synthesis, there is an inherent link between protein production and skeletal growth. Additionally, protein accounts for roughly 30% of bone mass so proper ribosome function is essential for bone development. Theoretically, any genotype alteration that alters ribosome function could induce phenotype changes in bone. Recently, a possible link between ribosomal

disruption and bone marrow failure has been established (Liu et al., 2006), validating this idea. Additionally, skeletal growth alterations were found in another RP mutant mouse model which displays kinetic defects in ribosome biogenesis (Oliver et al., 2004)

1.7 Rationale behind HIP/RPL29 disruption in mice

We are using a knockout mouse model to understand the role of HIP/RPL29 in mouse development and bone formation. A knockout mouse has the gene coding for one specific protein inactivated on both alleles. Assuming all other factors stay constant, a knockout mouse will produce all proteins except for the targeted protein.

To classify phenotypic differences in a genetically-modified mouse model, it is necessary to compare it to age-matched wild type samples, preferably littermates. Since mutant and wild type mice are typically raised under identical conditions, it is assumed that any significant differences between mutant and wild type mice are direct consequences behind the modification in the genome of the mutant animals. It is assumed that the role of the targeted protein is directly or indirectly responsible for these changes in phenotype.

1.7.1 Disruption of HIP/RPL29

Our laboratory created the first viable mutant mouse model lacking the gene coding for HIP/RPL29 (Kirn-Safran et al., 2007). Mice lacking this ribosomal protein display abnormal morphological features compared with wild type mice. Since HIP/RPL29-deficient mice only possess one single mutation, we know that any

significant phenotypic differences observed in mutants are consequences of the alteration of the *Hip/Rpl29* gene.

The *Hip/Rpl29* gene was disrupted using a homologous recombination targeting strategy in mouse 129S6 embryonic stem (ES) cells. By replacing the first three exons with a neomycin selection cassette (Figure 2), the *Hip/Rpl29* gene was successfully inactivated (Kirn-Safran et al., 2007). The modified ES cells were then isolated, injected into developing donor blastocysts obtained from C57Bl6/J mice and finally implanted in foster mothers. The chimeric offspring were bred with wild type (WT) 129S6 inbred mice to create HIP/RPL29 heterozygous (HET) mutants. The HET male and female offspring were then mated which resulted in the production of HIP/RPL29 WT, HET and null offspring (Figure 3). Southern blot analysis was used to confirm the genotypes of the initial progeny (Kirn-Safran et al., 2007).

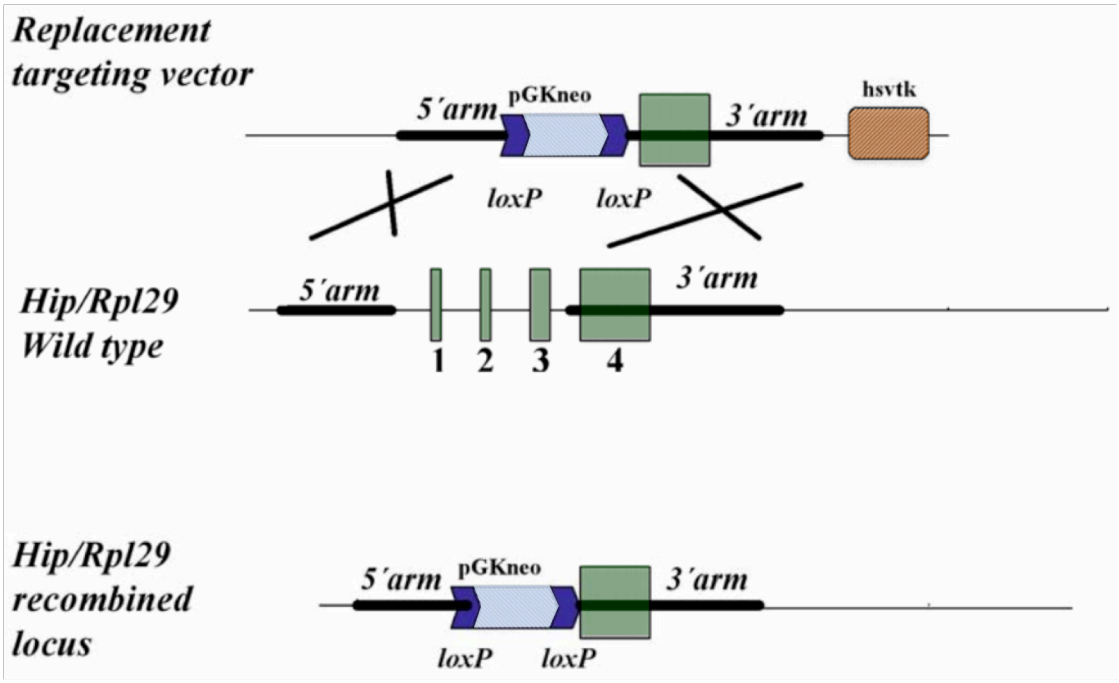

Figure 2: Strategy for targeting *Hip/Rpl29 gene*. Homologous recombination between the *Hip/*Rpl29 targeting vector and the wild type *Hip/*Rpl29 gene successfully disrupted the *Hip/Rpl29* gene. A neomycin selection cassette found on the replacement targeting vector replaced the first three exons (numbered 1-3) in the wild type gene (Adapted Kirn-Safran et al., 2007).

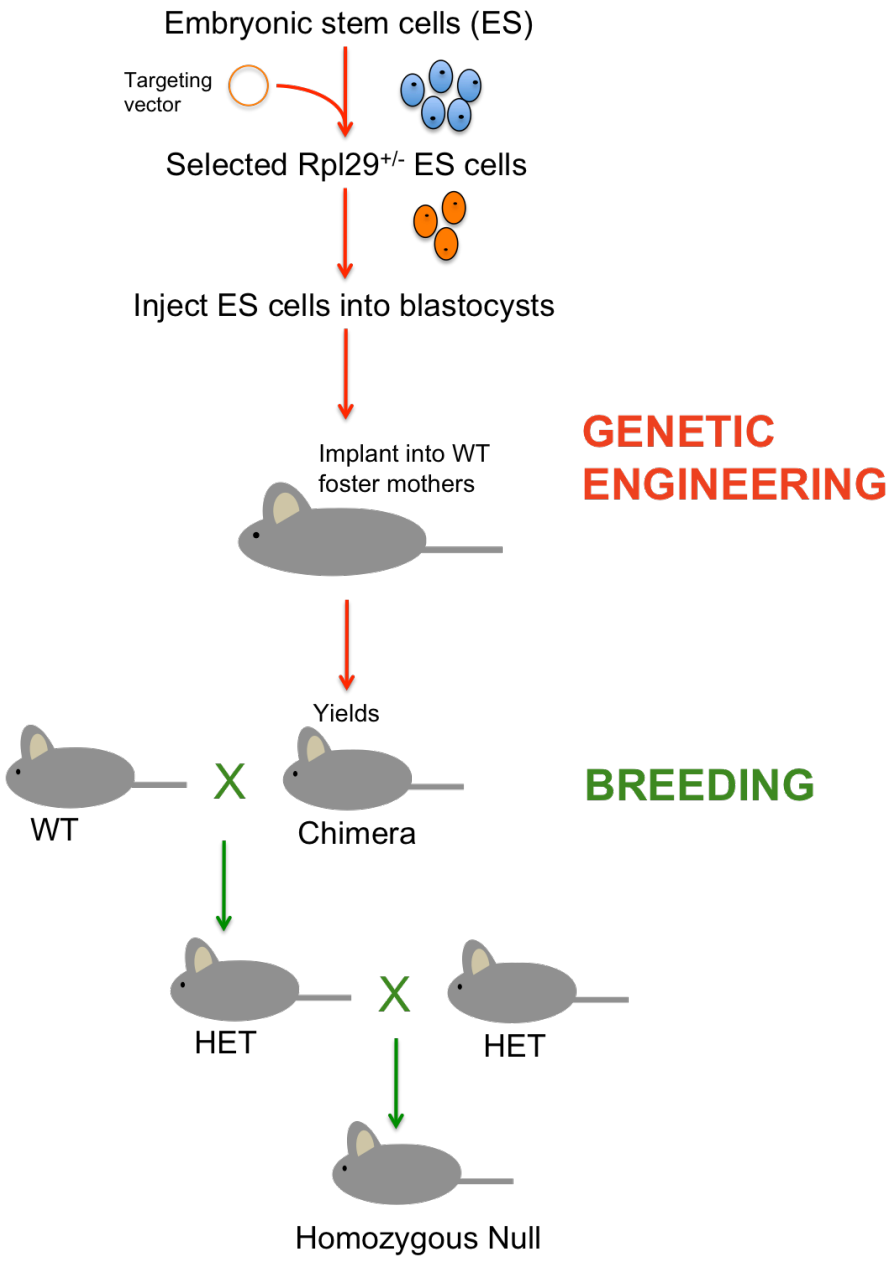

Figure 3: Creation of HIP/RPL29 null mice. Embryonic stem cells (ES) with a targeted disruption at the *Hip/Rpl29* gene were injected into a donor blastocyst. This complex was then implanted into the uterus of a foster mother. After birth, the chimeric offspring resulting from this procedure were crossed with wild type mice. The pups generated from this mating were HIP/RPL29-HET. Homozygous null mice resulted from the HET mouse intercrosses.

1.8 Global growth and skeletal changes resulting from HIP/RPL29 knockout

Growth deficiencies resulting from the deletion of the ribosomal protein HIP/RPL29 are apparent *in utero* around mid-gestation in two inbred mouse strains, 129S6 and C57B16/J. The apparent size discrepancy between null and WT fetuses was validated when a significant difference between the weights of the two populations was found.

After birth, the null phenotype is characterized by significant decreases in birth weight, organ and body size (Kirn-Safran et al., 2007). Postnatal lethality occurred in approximately half of the null progeny due to substantial developmental retardations.

Although HIP/RPL29-null mice achieve a normal lifespan, the described deficiencies persist throughout adulthood (See Figure 4). Additionally, null females that reach adult age exhibit delays in their sexual maturity. Although null female offspring are viable, they are essentially subfertile and null males are infertile (unpublished observations). Therefore, the population of null mice must be maintained by mating heterozygous male and female mice (Oristian et al., 2007). Given the reduced birth weight and body size of HIP/RPL29-deficient mice, it was anticipated that null bone exhibit decreased structural properties.

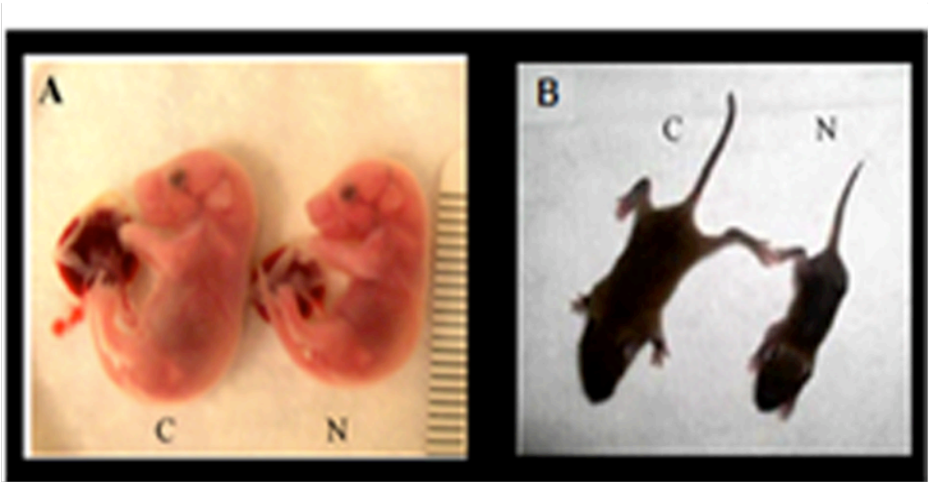

Figure 4: HIP/RPL29-deficient mice exhibit short stature phenotype. Delay in development is apparent in prenatal HIP/RPL29 null embryos (**A.** day 17.5) and one-week-old mice (**B**). Null HIP/RPL29 postnatal mice do not display any gross skeletal abnormalities, but show a reduction in axial and appendicular bone length. Adapted from Kirn-Safran et al., 2007.

1.8.1 Using beam theory to translate cortical bone properties into mathematics

Euler-Bernoulli beam theory, a simplified version of the linear theory of elasticity, describes the relationship between the applied load and deflection in a beam. Since the beam equation constituting beam theory describes forces and moments, it can be used to describe stresses. Assuming the femur can be treated like a horizontal beam, we can create hypothetical stiffness measurements of femurs of varying geometries thereby determining the effect of geometry on specific results from biomechanical testing. By altering the geometry and elastic moduli of these hypothetical femurs, we can accurately relate the relative importance of the macro and micro structural elements on bone stiffness measurements in the HIP/RPL29 model.

1.9 Objectives

In view of this information, it was hypothesized that the early defects due to protein deficiency in developing HIP/RPL29-null mice result in the bone fragility phenotype observed in later stages. To test this hypothesis, three specific aims have been addressed:

I. To compare the structural and material properties of bones of HIP/RPL29-deficient mice of different ages

II. To analyze the bone formation rates of RPL29 null mutant mice using dynamic histomorphometry and FT-IR

III. Determine the relative influence of the macro and microscopic changes in null bone on the bone fragility phenotype

Since HIP/RPL29-null stem cells responsible for bone formation exhibit reduced proliferation and global protein synthesis we anticipated a correlation between HIP/RPL29 deficiency and bone quality.

Chapter 2

MATERIALS AND METHODS

2.1 Experimental animals and statistics

Hip/Rpl29^{null} mice were created as described (Kirn-Safran et al., 2007) and backcrossed onto the C57BL6/J background. All animal care and handling was performed in accordance with the University of Delaware Institutional Animal Care and Use Committee approved guidelines. Statistical analysis was performed using a two-tailed Student's t-test, or with a two-way analysis of variance without replication.

2.2 Mouse Genotyping

2.2.1 Tail biopsies and DNA extraction

A 4-mm tail sample was collected from each mouse at approximately four weeks. All instruments were sterilized using a 10% bleach solution and 75% Ethyl Alcohol, and rinsed in distilled water prior to use. Upon collection, samples were frozen in individual eppendorf tubes.

DNA was extracted from the frozen tail samples using the REDExtract-N-Amp Tissue PCR Kit (Sigma Aldrich, St. Louis, MO.) according to the manufacturer's instructions. Briefly, the tail samples were mixed in extraction buffer and incubated in a 37°C waterbath for 15 minutes. To extract the DNA into the stock solution, tubes were heated to 95°C for 3 minutes. 50 µl of Neutralization Solution was added to each sample prior to storage at 4°C.

2.2.2 Polymerase Chain Reaction (PCR)

PCR tubes containing 1.3 µl PCR grade water, 2.5 µl REDExtract-N-Amp PCR Reaction Mix, 0.1 µl forward primer (0.4µM), .1 µl reverse primer (0.4 µM) and 1 µl tissue extract were prepared for each sample. Note that the JumpStart *Taq* antibody is present in the REDExtract-N-Amp PCR reaction mix, which is specific for hot start amplification. After placement in the thermocycler, all tubes were heated at 94°C for 30 seconds to denature the DNA by breaking the hydrogen bonds between all base pairs. The tubes were then cooled to 60°C for 30 seconds, which allowed the annealing of the forward and reverse primers to the denature DNA strands. New strands of DNA were synthesized using the single strands as templates during the extension step, which was conducted at 72°C for 1.5 minutes. This complete cycle was repeated 30 times and resulted in the exponential synthesis of DNA in each sample. After the cycles were completed, the samples were kept at 72°C for 10 minutes, which ensured that all remaining single stranded pieces of DNA were fully extended. All tubes were then stored at 4°C prior to gel electrophoresis.

2.2.3 Gel Electrophoresis

A 1.2% (w/v) agarose gel containing ethidium bromide was prepared with wells to load the amplified DNA. After placement in an electrophoresis apparatus, the gel was completely covered in 1x TAE Buffer, which provided a suitable environment for the creation of an electrical field. Five µl of the amplified DNA from each tail sample was transferred into individual wells on the agarose gel. Electrophoresis was conducted at 90 V for approximately 2-3 hours, or until the samples migrated halfway down the agarose gel. The gel was then placed above a UV transilluminator and the

band patterns from each sample were interpreted from a printed image to determine the genotype of each animal.

2.3 Dissection of femora and tibiae

Mice were sacrificed via CO_2 asphyxiation and cervical dislocation. Hind limbs were dislocated at the hip joint and mouse carcasses were stored at -4°C. Tibia and femur were separated and stored devoid of excess surrounding tissues. Unless otherwise stated, bone samples were kept in phosphate buffered saline (PBS) without calcium and magnesium at 4°C and thawed at 37°C for testing.

2.4 Micro-computed tomography (micro-CT) of mineralized tissue

2.4.1 Femora

Femurs harvested from 3 and 6 month male and female HIP/RPL29^{null} and control mice were scanned wet using a GE Healthcare eXplore Locus Pre-Clinical *in vivo* MicroCT Scanner ® (GE Healthcare, North America). Wrapped in a kimwipe saturated with 1x PBS, femurs were scanned for 2 hours at a resolution of 27 μm. Three-dimensional images were reconstructed with GE's reconstruction utility and analyzed using GE's Microview ® software. Cortical analysis was performed on a 3-mm × 3-mm × 2-mm (X × Y × Z) region of interest (ROI at midshaft, yellow in Figure 1) centered at the midpoint, exact to two decimal units, between the distal and proximal femoral heads. A different threshold value was selected for each scan using the histogram tool in Microview ®. Threshold values were approximately 1500 however they varied widely due to inherent variations in image in image quality among scans. The threshold was used to segment the selected ROI. This process

allowed for the separation of mineralized and non-mineralized voxels obtained in the region of interest (Ling et al., 2005). Geometric and structural measurements of the cortical bone in the selected ROI include bone mineral density (BMD), bone mineral content (BMC) and total cortical and bone marrow areas. The polar moment of inertia was obtained by summing the medial-lateral and anterior-posterior moments of inertia as described (Koller et al., 2003). Trabecular data was collected from a free form ROI generated 25 μm below the lowest point in the distal growth plate with the stereology feature of the Microview® Software. Statistical analysis was performed using unpaired two-tailed student's t-test.

2.4.2 Tibiae

Femurs and tibiae harvested from 5 month old HIP/RPL29-null and control mice were scanned wet in a custom built acrylic device which included a mineral standard material (SB3; Gammex RMI) and an air pocket used for calibration using a GE Healthcare eXplore Locus Pre-Clinical *in vivo* MicroCT Scanner® (GE Healthcare, North America). To increase the resolution to 20 μm, tibiae were scanned for approximately 6 hours instead of 2 hours. Three-dimensional images were reconstructed with GE's reconstruction utility as described for femora. Cross-sections from a specially selected 3 mm × 3 mm × 2 mm (X × Y × Z) region of interest of cortical bone immediately above the trochanter were exported and analyzed with custom code developed by Dr. C. Price (Department of Mechanical Engineering, University of Delaware) in MATLAB (MathWorks, v. 6.5). The isosurface tool was used to confirm our accuracy with respect to the region selection. The threshold function was selected using the histogram tool as described for femora. The

appropriate calibration value for our custom software was 0.0202. For the BMD calculations in our custom software, we used an average grayscale value of 3480, which was determined using the SB3 standard (1130mg/cc). Geometric and structural measurements of the cortical bone include bone mineral density (BMD - presented in Hounsfield Units), BMC and total cortical and bone marrow areas. Trabecular data was obtained for these samples as described in Section 2.4.1.

2.4.3 Teeth

Our collaborators at the Hospital for Special Surgery (New York City, NY) Drs. K. Verdelis and A. Boskey, extracted the right hemimandibles of 3 month-old *Hip/Rpl29*-null and age-matched WT mice and fixed them in 10% formalin. Samples were then placed in 70% ethanol and the molar-bearing segment was selected for analysis on a Scanco MicroCT35 scanner (Scanco Medical, Basserdorf, Switzerland) with a 6 μm voxel size as described (Sloofman et al., 2010).

2.5 Biomechanical testing

Three-point-bending tests were performed on male and female femoral (6 months) and tibial bones (5 months) using a mechanical MicroTester (Instron 5848, Norwood, MA) in collaboration with Dr. L Wang (Department of Mechanical Engineering, University of Delaware). A crosshead was monotonically lowered on the mid-shaft region of the samples with a speed of 0.01 mm/s, using a 10 N load cell, until failure. Bones were bent in the anterior-posterior (A/P) direction. Data points were collected every 0.001 s describing the load applied to the bone and the displacement of the crosshead. These curves were created and analyzed in Microsoft

Excel and used in conjunction with micro-CT data to calculate the ultimate force, ultimate moment, ultimate stress, work to failure, bone stiffness, bending rigidity (EI) Young's Modulus ($E = EI/I_{ML}$, where I_{ML} is the medial lateral moment of inertia), and the post-yield deflection (PYD). The PYD for each sample was calculated by taking the slope of the line connecting the initial point, and the yield point on the force vs. displacement curve. Bone stiffness, found by taking the slope of the linear portion of the curve, was used to calculate the bending rigidity of the sample (EI) by means of the simply supported beam equation, which can account for the error due to shearing displacement (Schriefer et al., 2005). The biomechanical testing set-up, along with a sample force-displacement curve, is shown in Figure 5.

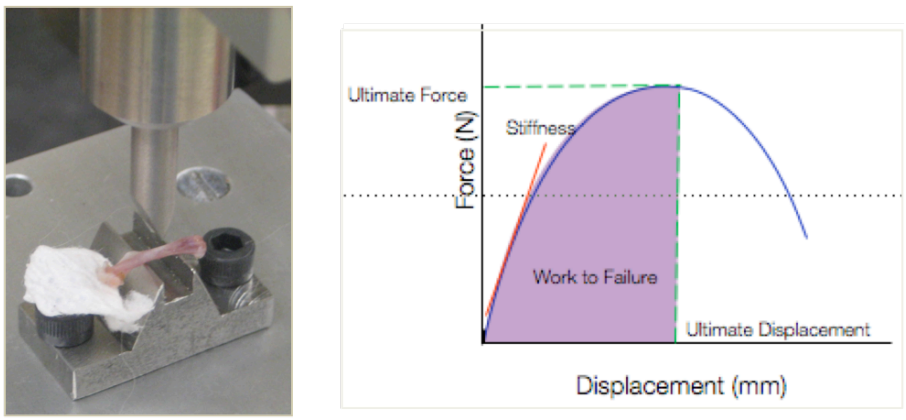

Figure 5: Interpreting data from three-point bending tests. Femora from six month-old control and null mice were loaded to failure at the diaphysis along the anterior-posterior axis. Force-displacement curves were generated for each sample (see example of a standard sample force displacement curve on right). From these curves, mechanical properties (stiffness, rigidity, ultimate load), structural properties (dimensions, areas, moment inertia) and material properties (E, mineralization) were calculated using Microsoft Excel. The ultimate force and ultimate displacement are displayed with green dashed lines while the line used to calculate the stiffness is shown in red. The area under the curve corresponding to the work to failure is highlighted in purple.

2.6 *In-vivo* cyclic axial loading

To determine if reduced capacity to synthesize large volumes of proteins modifies bone anabolic response to mechanical load, the left tibiae of 21-week-old HIP/RPL29-null mice (n=3) and age-matched wild type controls (n=6) were loaded on an Instron machine at 20% maximal load (5.6 N for control and 4.1 N for null mice), 0.5 Hz for 50 cycles/day, with a five-second rest period inserted between two cycles for two weeks. Isofluorane anesthesia was administered to mice throughout the entire mechanical loading procedure through a fitted nose cone. Loading commenced on day

1 of the study, and ended on day 14. Intraperitoneal injections of calcein (15mg calcein/kg) were given to all mice on days 8 and 15, twice per day to track mineral apposition rates in cortical bone throughout the duration of the mechanical loading study. A schematic of our protocol is shown in Figure 6.

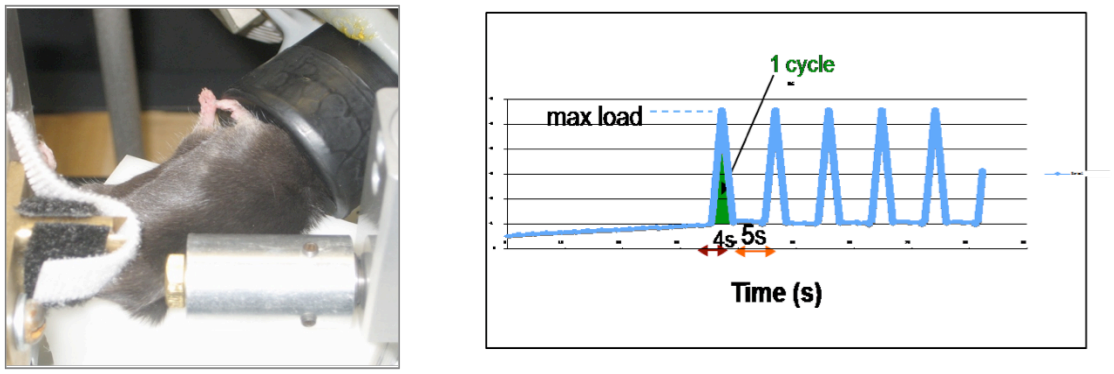

Figure 6: Mechanical loading of HIP/RPL29-deficient and control tibiae. Loading of control (max load 5.6 N) and null mice (max load 4.1 N) was performed on live animals as described by Fritton and colleagues (2005). 21 week -old mice were anesthetized under isofluorane while cyclic axial compressions of 1/4 Hz were applied with a 5 second rest period in between each cycle (See force-time curve on right). The left foot was secured in a brass platen. The contralateral limb was not loaded, thus serving as an internal control. These loading cycles mimic stress from locomotion.

2.6.1 The loading apparatus

The Instron machine was oriented horizontally with respect to the ground. A custom-made brass platen was secured to the base of the machine. The left foot of each mouse was secured in a custom-made brass platen that sat on a 10 N load cell, shown in Figure 6. The left knee was secured in a brass cup. Pressure was applied to

the tibia through the compression and extension of the actuator on the mouse knee. The left hindlimb was situated such that the tibia was parallel to the ground, and the ankle was flexed at approximately 45º. The right hindlimb remained unloaded and thus served as an internal control.

2.6.2 Assessing impact of mechanical loading

The cortical bone microstructure and material properties of the non-loaded and loaded tibiae of both HIP/RPL29-null and WT mice were analyzed using Micro-CT and three-point-bending tests respectively. Dynamic histomorphometry was used to measure mineral apposition rates and growth along the endosteal and periosteal perimeter in loaded and non-loaded samples (See Figure 7).

Since our mechanical loading protocol was only expected to induce slight structural changes in cortical bone, we altered our micro-CT protocol to increase the resolution of our three-dimensional images. All Scans had a resolution of 21 μm. Tibiae were scanned seven at a time in a custom made acrylic holder which also held an SB3 hydroxyapatite standard material and an air hole which were used for the calibration of the mini-volume, which was used to reconstruct the individual samples. Samples were reconstructed using the GE Microview Software® and analyzed using custom software as described in Section 2.4.2

To increase the accuracy of the analysis of our structural data, the method of cortical analysis was also improved. Instead of analyzing a 3×3×2 ROI at the mid-diaphysis using GE Microview Software®, we exported the entire ROI, which contained the individual slice data throughout the entire region, to custom-built

software described previously. Trabecular analysis was performed as described in Section 2.4.1.

Dynamic Histomorphometry was performed under the supervision of Dr. C. Price and Dr. L. Wang (Department of Mechanical Engineering, University of Delaware), in collaboration with the Mechanical Engineering department at UD. Cross sections from the mid-diaphysis of the tibiae were cut using a diamond saw and imaged using epifluorescence microscopy and post processed in custom-made MATLAB codes following standard histomorphometry criteriae. A sample processed cross-section is shown in Figure 7.

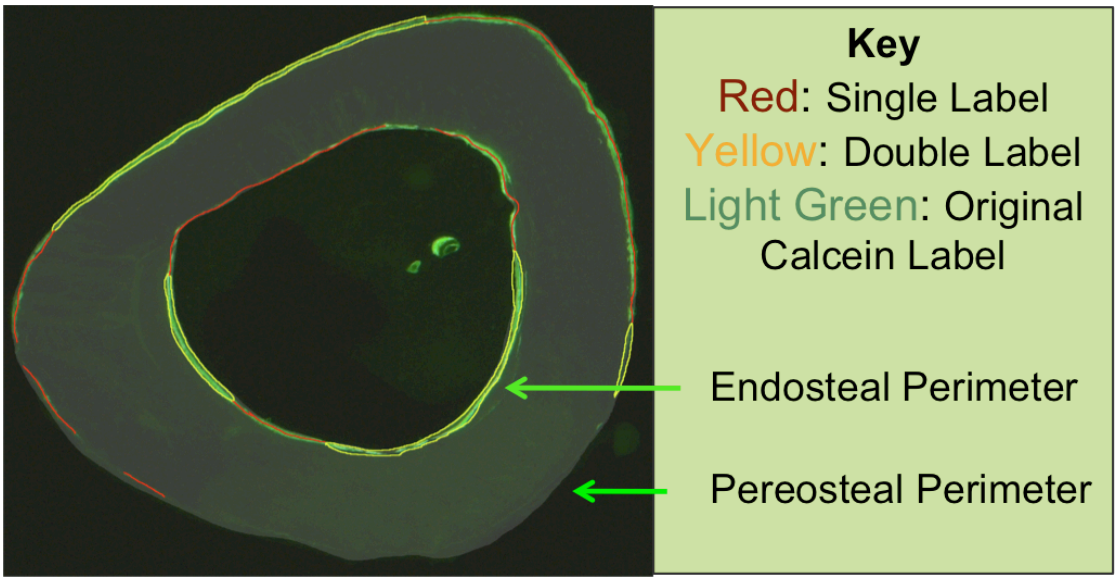

Figure 7: Guide to interpreting data from dynamic histomorphometry. Intraperitoneal injections of calcein were administered on days 8 and 15, twice per day. After histological processing without decalcification, the growth on loaded and non-loaded tibia was measured in both the periosteal (outer) and endosteal (inner) perimeters. By measuring the distance between the labeled surfaces from either the endosteal or periosteal perimeters, mineral apposition rates were calculated. This procedure was completed in loaded and non-loaded control and null tibiae (cross section of #1823 shown above).

2.7 Bone and teeth composition analysis

2.7.1 Tibiae

Sections (2-3 μm thick) of all WT and HIP/RPL29 null bone samples were examined using Fourier Transform Infrared Imaging (FTIRI; Perkin Elmer Spotlight 300 Imaging system, Perkin Elmer Instruments, Shelton, CT, USA in collaboration with Dr. A. Boskey at the Hospital for Special Surgery, New York City, NY. Cortical

and trabecular bone areas were scanned separately, and 3-5 areas of each type of bone were examined per bone. Because no significant difference was observed between genders for most of the bone parameters examined, male and female FTIRI data were combined into either a WT or a HIP/RPL29-null category ($n \geq 8$ for each group). Spectroscopic profiles were created for each sample as described by our collaborators (Sloofman et al., 2010). The following spectroscopic parameters were determined: mineral-to-matrix ratio [v1, v3 PO4 band (900-1,180 cm^{-1}) / amide I band (1596-1712 cm^{-1})], collagen crosslink ratio (1660 cm^{-1}/1690 cm^{-1}), carbonate-to-mineral ratio [carbonate band (852-900 cm^{-1})/ v1, v3 PO4 band 900-1,180 cm^{-1}], and crystallinity (1030 cm^{-1}/1020 cm^{-1}), a value corresponding to the crystallite size and perfection determined by X-ray diffraction (Sloofman et al., 2010).

All spectroscopic results were then expressed as histograms, detailing the mean values of pixel distribution for the mentioned parameters and standard deviations. Corresponding color-coded hyperspectral images (where x, and y are the locations on the specimen and z the intensity of the peak or calculated ratio at each pixel) were generated concurrently by ISYS for all parameters (Sloofman et al., 2010).

2.7.2 Teeth

The left hemimandibles of WT and null female animals were partially fixed in 70% ethanol and were used for the FTIRI analysis of the molar dentin ($n \geq 4$) by our collaborator at the Hospital for Special Surgery (Dr. K. Verdelis, HSS Hospital, New York City, NY). Samples were prepared and scanned as described by Sloofman et al, 2010. Bone, background and enamel remnant areas in the scanned fields were

hidden which allowed for the analysis of mineral and matrix properties from the molar crown dentin images (Sloofman et al., 2010).

2.8 Mathematical modeling of cortical bone

MATLAB code was used to solve the equations of beam theory. The overarching idea in this simulation is to mimic the applied loading during the three-point-bending tests to simulate the effect of bone geometry on stiffness measurements. Both Model 1 and Model 2 assume:

1. Femur has no mass
2. Femur is symmetrical
3. Bone is devoid of any excess tissue
4. EI and stiffness is constant throughout the tissue
5. Bone is treated as a static object

Femoral deflections were assumed to satisfy the governing equation:

$$EI\frac{\partial u}{\partial x'^4} = p\delta(x') \tag{1}$$

where , x is the spatial coordinate and p represents the applied force on the femur. The delta function, otherwise known as the impulse function, was used in conjunction with the p parameter to apply a point force on the hypothetical femur. The function $u(x)$ measures the deflection at location x.

2.8.1 Non-dimensionalization

To non-dimensionalize our problem we defined the following dimensionless variables:

$$x = \frac{x'}{L}$$
$$u = \frac{u'}{U} \tag{2}$$

where L is the total length of the sample and U is to be determined. The governing equation, presented in its non-dimensionalized form is:

$$\frac{EI}{L^4} U u_{xxxx} = p\delta(x) \tag{3}$$

Setting $U = \frac{pL^4}{EI}$ we obtain:

$$u_{xxxx} = \delta(x) \tag{4}$$

2.8.2 Model 1

The first version of our software only considers the femur as a 4.5-mm region of cortical bone, which has a non-dimensionalized length of 1. Therefore, in this iteration, it is assumed that HIP/RPL29-null and control samples have the same geometry. The chosen region corresponds to the femoral mid-shaft that lies between the pins on the three-point-bending test device. The impulse is applied at position(s) $x = x_0$, where $-0.2 \le x_0 \le 0.2$. In the first model, the governing equation is solved only once per sample since we are only considering one region in the femur. This solution is:

$$u(x) = \begin{cases} a_0 x_0^{\,3} + a_1 x_0^{\,2} + a_2 x_0 + a_3, & -1/2 < x < x_0 \\ b_0 x_0^{\,3} + b_1 x_0^{\,2} + b_2 x_0 + b_3, & x_0 < x < 1/2 \end{cases} \tag{5}$$

Since a discontinuity is present in the fourth derivative at $x=x_0$, the solution was broken into multiple components to accurately describe its behavior. The

$x=0$ mark represents the center of our mathematical femur. The ends of the femur lie at the $x = \pm ½$.

The boundaries of this region, at $x = \pm ½$ are treated as pinned. This implies the boundary condition:

$$u(x) = \frac{\partial^2 u}{\partial x^2} = 0 \tag{6}$$

Since the solution of this system of equations is continuous, we also know that $u_L(x_0) = u_R(x_0)$. The solution u is also continuous in the first and second derivatives at x_0. The jump condition in on the third derivative is obtained by integrating:

$$\int_{-\varepsilon}^{\varepsilon} u_{xxxx} = \int_{-\varepsilon}^{\varepsilon} \delta(x) \tag{7}$$

so that $6b_0 - 6a_0 = 1$. After all constants were determined, we solved for u' (the slope of the hypothetical force-displacement curve) using equation (2) and defining U as we did in equation (3), we obtain:

$$pL = \frac{EI}{L^3 a_3} u'(0) \tag{8}$$

where $\frac{EI}{L^3 a_3}$ is the slope of our hypothetical force-displacement curve, otherwise known as our stiffness calculation. By varying the position of the impulse on the cortical region, we can obtain multiple stiffness calculations for each gender and genotype combination.

2.8.3 Model 2

To study the effect of bone geometry on stiffness measurements at the femoral mid-shaft, we added distal and proximal sections to the beam representing cortical mid-shaft. Therefore, to build either a control or null femur, we were concatenating three beams into one non-dimensionalized hypothetical null or control femur. A schematic of our methodology is presented in Figure 8.

To simplify our calculations, the distal (end near knee joint) and the proximal (near hip joint) ends measured a non-dimensionalized length of 0.8125, corresponding to 3.75-mm. These values were approximated to mimic the length of control samples. As in model 1, the inputs of hypothetical null and control femora differed only in their EI value.

The deflection was only measured in the center piece, corresponding to the mid-shaft, of each femur. Additionally, we had to add boundary conditions at the edges of each section. The ends of the cortical region had the same pinned boundary conditions described in equation (6). The free ends of the distal and proximal ends had free boundary conditions defined as:

$$\frac{\partial^2 u}{\partial x^2} = \frac{\partial^3 u}{\partial x^3} = 0 \tag{9}$$

Additionally, equation (7) applies to the second model giving us condition $6b_0\text{-}6c_0=1$. Given these new boundary conditions, our new solution takes a slightly different form:

$$u(x) = \begin{cases} a_0 x_0^{\,3} + a_1 x_0^{\,2} + a_2 x_0 + a_3, & -\frac{1}{2} < x < -\frac{3}{16} \\ b_0 x_0^{\,3} + b_1 x_0^{\,2} + b_2 x_0 + b_3, & -\frac{3}{16} < x < x_0 \\ c_0 x_0^{\,3} + c_1 x_0^{\,2} + c_2 x_0 + c_3, & x_0 < x < \frac{3}{16} \\ d_0 x_0^{\,3} + d_1 x_0^{\,2} + d_2 x_0 + d_3, & \frac{3}{16} < x < \frac{1}{2} \end{cases} \tag{10}$$

where a_0-a_3 describe the hip, b_0-b_3 describe the region of cortical bone between the proximal end and the impulse, c_0-c_3 describe the region between the impulse and the distal end, and d_0-d_3 describe the distal end. Note that the solution should be continuous at x_0 in the first and second derivatives. Additionally the boundaries at the proximal end/mid-shaft and mid-shaft/distal end are continuous in the first and second derivatives. Given this extra information, it is possible to solve for all of the constants defined in equation (10). It should be noted that the a_3 term written in all of the equations describing Model 1 corresponds to $c_3 + c_2 x_0$ where $c_2 x_0$ is a correction term accounting for the fact that $b_3 \neq c_3$

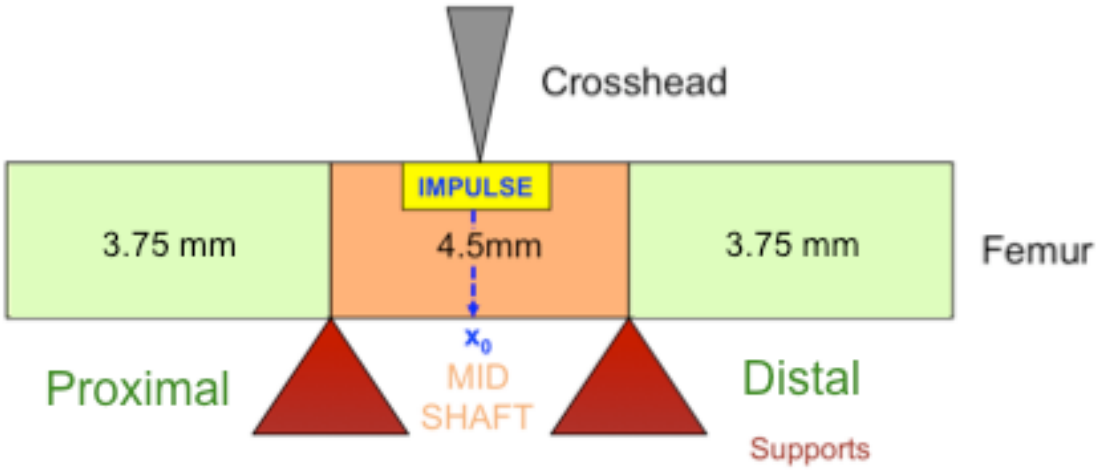

Figure 8: Schematic for mathematical modeling. The femur was approximated by concatenating three distinct blocks of differing lengths. The delta function, otherwise known as the impulse function, was used to simulate the force exerted on the femur from the crosshead at $x = x_0$. Note that the first model iteration disregarded the presence of the proximal and the distal to simplify the calculations.

Chapter 3

RESULTS

3.1 *Hip/Rpl29* gene deletion alters bone growth

3.1.1 HIP/RPL29 null bone displays decreased structural properties

HIP/RPL29-deficient mice exhibit a short stature phenotype from birth through adulthood. Generally, null mice weigh 25% less than their wild type counterparts and they can be up to 50% smaller than their littermates at weaning age (Kirn-Safran et al., 2007). At the macroscopic level, HIP/RPL29-null femora and tibiae are 7% shorter and they exhibit a 30% decrease in wet weight (Oristian et al., 2009). Therefore, we can conclude that HIP/RPL29 deletion results in global growth decrease of the mouse skeleton.

Results from the microCT of 6 month femora are summarized in Table 1 and were reported by Oristian et al. (2009), and confirmed global structural changes in the cortical and trabecular bone of HIP/RPL29-null femora. These changes were also gender-specific. Most notably the cortical area in HIP/RPL29-deficient femora, which is the average amount of cortical bone in a cross sectional area, decreased by 19.0% in female samples ($p < 0.05$ WT 0.99-mm^2, null 0.80-mm^2), while the average cortical area was preserved in male samples. This observation correlates with the observed 7.6% decrease in cortical width in female samples whereas the cortical width in male samples remains unchanged. Additionally, the preservation of cortical area in male samples was coupled with a 38% decrease in marrow area (null male vs. control male,

$p < 0.05$) whereas only a 17.2% ($p<0.05$) decrease was found in female null samples when compared to gender-matched controls. A visual interpretation is shown in Figure 9, along with representative cortical and trabecular regions of interest for null and control samples. Interestingly, the BMD remains unchanged in female samples despite the observed decreases in cortical area. In contrast, an increase in BMD of 4.3% was observed in male null samples.

Male and female null femurs also exhibited significant reductions in their anterior-posterior (AP) and medial-lateral (ML) diameters. Null females exhibited significant decreases of 9.7% and 9.9% and null males exhibited significant decreases of 14.8% and 13.2% in their AP and ML diameters, respectively. Likewise, female and male samples exhibited 9.2% and 13.9% decreases in the outer perimeter and 9.6% and 21.3% decreases in the inner perimeter, respectively. The decreases in the diameter lengths and perimeters of null femora resulted in 18.3% and 24.9% reductions in the total tissue area of female and male null femora in the specified region of analyzed cortical bone.

HIP/RPL29 knockout induced minimal changes in the trabecular thickness, trabecular number and trabecular separation in female femora. However, significant decreases in BMD, tissue mineral density (TMD), and total volume of 13.4%, 9.1%, and 16.6% ($p < 0.05$) were observed in null samples when compared to age-matched controls. Male null femora showed an 18.9% increase in the bone volume to total volume ratio and a 25% decrease in total volume. In contrast, trabecular thickness, trabecular number, trabecular separation, BMD and TMD was observed in HIP/RPL29 null males.

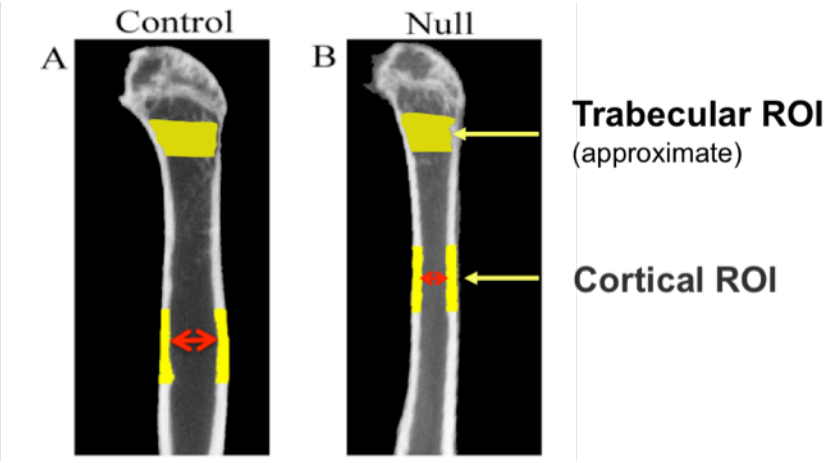

Figure 9: Altered structure of HIP/RPL29-null bone is detectable via micro-CT. The decrease in bone marrow area in mutant animals is obvious in the diaphysis region corresponding to the cortical region of interest highlighted in yellow (micro-CT measurements summarized in Table 1). Trabecular analysis was performed .27 μm below the growth plate. Adapted from Oristian, 2007.

Table 1: Comparative micro-CT analysis

A. Cross-sectional cortical properties at femoral mid-shaft

	Females		*Males*	
	Control	Hip/Rpl29$^{-/-}$ % reduction vs. control	Control	Hip/Rpl29$^{-/-}$ % change vs. control
Outer Perimeter (mm)	4.67 (+/-0.144)	4.24 (+/-0.258) -9.2%	5.53 (+/-0.506)	4.76 (+/-0.188) -13.9%
Inner Perimeter (mm)	3.03 (+/-0.145)	2.74 (+/-0.293) -9.6%	4.08 (+/-0.568)	3.21 (+/-0.191) -21.3%
Marrow Area (mm^2)	0.651 (+/-0.063)	0.539 (+/-0.115) -17.2%	1.13 (+/-0.312)	0.699 (+/-0.074) -38.1%
Cortical Area (mm^2)	0.986 (+/-0.050)	0.798 (+/-0.071) -19.0%	1.08 (+/-0.222)	0.96 (+/-0.059) -11.0% n.s.
A/P bone diameter (Depth ,mm)	1.546 (+/-0.072)	1.396 (+/-0.065) -9.7%	1.759(+/-0.213)	1.499(+/-0.074) -14.8%
M/L bone diameter (Width ,mm)	2.201 (+/-0.06)	1.982(+/-0.162) -9.9%	2.685(+/-0.218)	2.329(+/-0.135) -13.2%
Cortical width, (CTW, mm)	0.304 (+/-0.019)	0.281 (+/-0.016) -7.6%	0.296(+/-0.027)	0.299(+/-0.014) No change.
I_{ML} (=I_{xx}, mm^4)	0.277 (+/-0.035)	0.176 (+/-0.042) -36.5%	0.463(+/-0.068)	0.234 (+/-0.048) -49.5%
I_{AP} (=I_{yy}, mm^4)	0.566 (+/-0.068)	0.359 (+/-0.103) -36.6%	0.947(+/-0.204)	0.521(+/-0.074) -55%
BMD (mg/cm^3)	883 (+/-21)	861 (+/-26) -2.5%	976 (+/-22)	1018 (+/-19) +4.3%
Total tissue area (mm^2)	1.64(+/-0.1)	1.34(+/0.15) -18.3%	2.21(+/-0.34)	1.66(+/-0.12) -24.9%

B. Trabecular properties of distal femora

	Females		*Males*	
	Control	Hip/Rpl29$^{-/-}$ (%change vs. Control)	Control	Hip/Rpl29$^{-/-}$ (%change vs. Control)
BV/TV	0.177(+/- 0.029)	0.158(0.028) -10.7%	0.254 (+/-0.029)	0.302 (+/- 0.041) +18.9%
Trabecular thickness (Tb. Th, mm)	67.8 (+/- 9.8)	59.4 (+/- 9.9) -12.4%	70.8 (+/- 5.8)	75.9 (+/-6.2) +7.2%
Trabecular number (Tb. N/mm)	2.65 (+/-0.21)	2.66 (+/-0.24) No change	3.62 (+/- 0.48)	3.96 (+/-0.37) +9.6%
Trabecular Separation (Tb. Sp, mm)	312.3 (+/- 32.1)	318.7 (+/- 35.9) No change	210.2 (+/-39.5)	178.4 (+/-28.8) -15.1%
BMD (mg/cm^3)	247 (+/-23)	214 (+/-21) -13.4%	347 (+/-13)	363 (+/-35) +4.6% n.s.
Total volume (TV, mm^3)	2.345 (+/-0.125)	1.956 (+/- 0.19) -16.6%	3.318 (+/- 0.5)	2.49 (+/- 0.19) -25%

All the % change indicated in bold are statistically significant $p<0.05$. n.s, non-significant. Data are shown as mean ±standard deviation. BV, bone volume; TV, total volume; BMD, bone mineral density. I_{ML}, and I_{AP} are the medial-lateral and the antero-posterior moment of inertia, respectively.

3.1.2 HIP/RPL29-null bone displays increased material properties

Figure 10 summarizes the changes in HIP/RPL29 null bone material properties and were previously reported (Oristian et al., 2007). A significant increase in elasticity was observed in male null femurs ($p < 0.05$, null versus controls) while the corresponding increase in null female samples was not statistically significant when compared to gender-matched controls. However, females exhibited a significant decrease in EI ($p < 0.05$), a measure of bending rigidity, whereas male samples did not. This observation is also consistent with the preservation of cortical thickness only in null males. However, only female femora displayed significant increases in stiffness, which are presented in Figure 10. Despite the maintenance of geometrical properties and the increase in BMD in male null samples compared with wild type controls, both male and female null samples could not resist comparable forces to wild type samples at failure. Male and female null samples withstood 17.5% and 14.7% less force compared with age and gender-matched wild type controls ($p < 0.05$). However, the BMD in 6-month null male femurs increased while the post-yield displacement (PYD) decreased (data not shown) when compared to age-matched controls, so this assertion cannot be made without further examination.

During biomechanical testing, it is also possible that the force distribution was altered in genetically modified samples due to their inherent size differences. For instance, it is plausible that a larger object can absorb more force due to its larger size. Therefore, any micromechanical changes in HIP/RPL29-deficient bone measured using mechanical loading may be due to altered material properties and/or any measured decrease in size and sample weight.

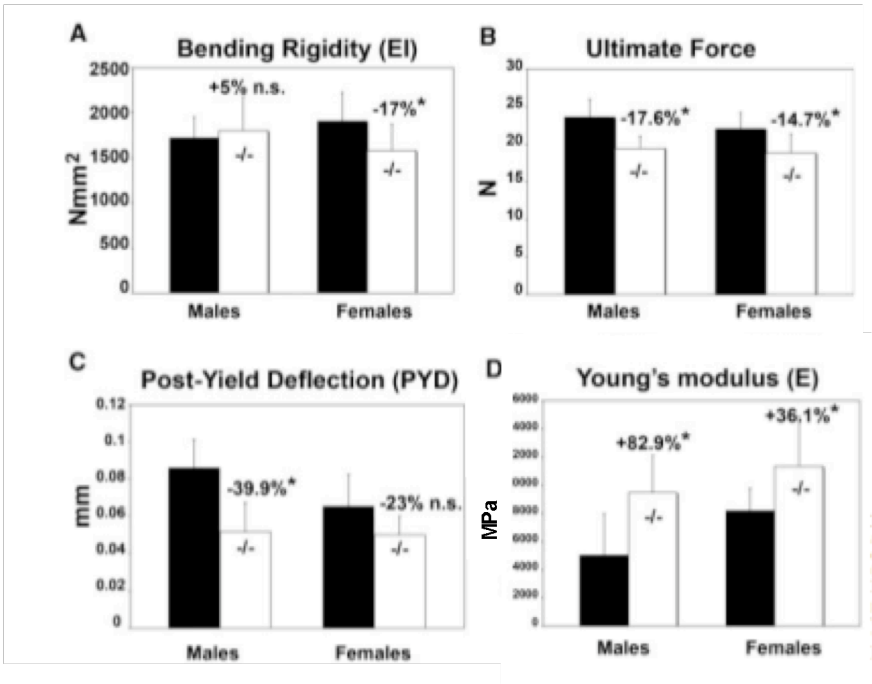

Figure 10: HIP/RPL29-deficient mice exhibit altered material properties. EI and ultimate force of HIP/RPL29-null and control femurs are shown. The elastic modulus (E) was calculated by dividing EI by the medial lateral moment of inertia reported in Table 1. Adapted from Oristian et al., 2009

3.1.3 Light mechanical loading fails to induce an anabolic response in bone tissue in HIP/RPL29-deficient and control tibiae

To determine the impact of sub-cellular constituents on bone structure and composition, we attempted to measure the bone anabolic response to mechanical loading. By comparing the ability of both HIP/RPL29 null and control bone to mount a response to mechanical load, we hoped to elucidate the distinction between the role of the macrostructure and cellular mechanisms involved in the maintenance of structural defects during adulthood in HIP/RPL29-deficient bones. Since HIP/RPL29 deletion alters bone structure, we can assume that the cellular activity regarding bone maintenance in HIP/RPL29-deficient samples is already altered. Under short periods of mechanical loading, we hypothesized that existing differences in the cellular mechanisms behind the maintenance of cortical and trabecular bone would be exacerbated.

Unfortunately, neither control nor HIP/RPL29-null bones responded to mechanical loading by apposing new bone. Due to machine limitations, we had to change our loading frequency from 1 Hz to 0.25 Hz thereby loading the sample once every four seconds instead of once per second. Results from dynamic histomorphometry, shown in Table 2, indicate that the mechanical loading had no effect on the osteoblast activity in both control and in null bone. For example, significant differences were not observed between loaded and non-loaded null tibiae in cortical area, total area, cortical thickness and both the periosteal and endosteal mineral apposition rates ($p>0.05$; Percentages reported in Table 1). Loaded and non-loaded controls differed only in their percent periosteal single label and percent

periosteal labeled surface (+33.5% and +41% respectively; $p<0.05$). However these changes in null samples did not lead to a significantly altered periosteal mineral apposition rate in null animals (-29.8%; $p>0.05$). Note that significant decreases in the cortical area (-16.8%; $p<0.05$), polar moment of inertia (-39.9%; $p<0.05$), total area (-21.49%; $p<0.05$) and marrow area (-30.0%; $p<0.05$) were observed, consistent with 6-month samples. Micro-CT and three-point-bending testing, conducted after loading commenced, were not sensitive enough to identify any subtle structural changes in loaded samples (data not shown).

Table 2: Mechanical loading induces minimal changes in 5-month-old control and HIP/RPL29-null femora

A. Dynamic Histomorphometry

	Loaded WT	Non-loaded WT	Loaded Null	Non-loaded Null
Cortical Area	0.687 (+/-0.073)	0.657 (+/-0.035)	0.629 (+/-0.096)	0.546 (+/-0.034)
Max rectangular Moment of Inertia	0.121 (+/-0.049)	0.094 (+/-0.024)	0.106 (+/-0.064)	0.051 (+/-0.003)
Min rectangular Moment of Inertia	0.067 (+/-0.008)	0.061 (+/-0.009)	0.059 (+/-0.026)	0.043 (+/-0.006)
Polar Moment of inertia	0.188 (+/-0.055)	0.155 (+/-0.032)	0.165 (+/-0.090)	0.093 (+/-0.009)
Total Area	1.084 (+/-0.103)	1.013 (+/-0.096)	0.982 (+/-0.238)	0.795 (+/-0.037)
Marrow Area	0.397 (+/-0.047)	0.356 (+/-0.071)	0.353 (+/-0.156)	0.249 (+/-0.016)
Avg. Cortical Thickness	0.209 (+/-0.019)	0.219 (+/-0.016)	0.195 (+/-0.032)	0.213 (+/-0.010)
Percent Periosteal Single Label	30.130 (+/-0.081)	45.320 (+/-0.049)	48.530 (+/-0.091)	57.480 (+/-0.325)
Percent Periosteal Labeled Surface	26.880 (+/-0.087)	45.540 (+/-0.135)	51.480 (+/-0.139)	62.100 (+/-0.221)
Periosteal Mineral Apposition Rate	0.001 (+/-0.001)	0.002 (+/-0.000)	0.002 (+/-0.001)	0.002 (+/-0.001)
Percent Endosteal Single Label	25.140 (+/-0.148)	38.940 (+/-0.162)	42.590 (+/-0.163)	29.320 (+/-0.097)
Percent Endosteal Labeled Surface	56.820 (+/-0.142)	64.200 (+/-0.179)	38.930 (+/-0.254)	53.360 (+/-0.366)
Endosteal Mineral Apposition Rate	0.002 (+/-0.0003)	0.002 (+/-0.0004)	0.001 (+/-0.001)	0.002 (+/-0.001)

Data are shown as mean ±standard deviation.

B. Percent changes among loaded and non-loaded WT and nulls.

	Percent change (relative to controls)			
	LW VS UW	LN VS NN	LN VS LW	UN VS UW
Cortical Area	4.57%	15.12%	-8.49%	**-16.88%***
Max rectangular Moment of Inertia	29.49%	110.87%	-12.18%	**-46.07%***
Min rectangular Moment of Inertia	9.30%	37.40%	-12.43%	**-30.33%***
Polar Moment of inertia	21.52%	77.26%	-12.27%	**-39.86%***
Total Area	6.98%	23.40%	-9.44%	**-21.49%***
Marrow Area	11.43%	41.53%	-11.09%	**-30.00%***
Average Cortical Thickness	-4.45%	-8.84%	-6.86%	-2.37%
Percent Periosteal Single Label	**-33.53%***	-15.57%	**61.09%***	26.83%
Percent Periosteal Labeled Surface	**-40.97%***	-17.11%	91.53%	36.38%
Periosteal Mineral Apposition Rate	-29.82%	4.05%	32.72%	-10.48%
Percent Endosteal Single Label	-35.43%	45.27%	69.41%	-24.70%
Percent Endosteal Labeled Surface	-11.49%	-27.03%	-31.48%	-16.88%
Endosteal Mineral Apposition Rate	18.71%	-7.77%	-43.57%	-27.37%

*$p<0.05$. Non-loaded samples serve as internal controls for the loading experiments. WT samples serve as controls for comparisons between genotypes.

3.2 *Hip/Rpl29* gene deletion alters micro-structural composition

3.2.1 HIP/RPL29-deficient trabecular bone exhibits an increase in the mineralizing surface

Static and dynamic histomorphometry was performed on the trabecular bone in the femurs of four-month HIP/RPL29-null and age matched controls. We chose to use younger samples for this section since trabeculae are harder to detect in aging adult bone (Sloofman et al., 2010).

With the exception of a significant reduction in the mineralizing surface in HIP/RPL29-null femurs (-37.5%; null vs. controls, $p < 0.05$), histomorphometric data showed no significant differences in any measured trabecular properties (Table 3). Consistent with our previous observations performed using 6-month old bone, the average bone volume to total volume ratio decreased by 15.6% in null animals, however, this change was not statistically significant. This change was accompanied by non-significant decreases in trabecular thickness (-13.9%; null vs. controls, $p>0.05$) and trabecular spacing (-6.48%; null vs. controls; $p > 0.05$). The altered trabecular phenotype in HIP/RPL29 null mutants is maintained throughout the life of the animal.

Results from dynamic histomorphometry, also presented in Table 3, indicate a significant decrease in the mineralizing surface in null trabecular bone (-37.5%, $p < 0.05$) when compared to controls; although this significance disappears when the mineralizing surface is normalized with respect to the bone surface (MS/BS; null vs. control; -7.1%, $p>0.05$). Additional non-significant decreases in the mineral

apposition rate (MAR; -11.7%, p> 0.05) and the bone formation rate (BFR/BS; -18.2%, p > 0.05) were observed in HIP/RPL29-deficient trabecular bone.

Table 3: Static and dynamic histomorphometry of 4 month old trabecular bone

	Controls	*Hip/Rpl29$^{-/-}$*
BV/TV	10.28 (+/- 6.88)	8.67 (+/- 3.86)
Bone Perimeter (BS) mm	6.01 (+/- 4.53)	6.03 (+/- 1.45)
BS/BV (mm-1)	62.96 (+/- 10.48)	69.33 (+/- 14.96)
BS/TV (mm-1)	5.57 (+/- 2.45)	5.62 (+/- 1.69)
Trabecular Thickness (μm)	34.87 (+/- 12.49)	30.01 (+/- 7.04)
Trabecular Number (mm-1)	2.78 (+/- 1.23)	2.81 (+/- 0.85)
Trabecular Space (μm)	385.69 (+/- 191.54)	360.70 (+/- 158.94)
Mineralizing surface/MS (mm)	3.65 (+/- 1.13)	2.28 (+/- 1.22)*
MS/BS	35.56 (+/- 9.33)	33.03 (+/- 13.10)
Mineral Apposition Rate (MAR) μm/day	1.54 (+/- 0.29)	1.36 (+/- 0.43)
Bone Form Rate (BFR/BS) μm/day	0.55 (+/- 0.22)	0.45 (+/-0.21)

p< 0.05; Controls consist of both WT and HIP/RPL29$^{+/-}$ mice. n≥4.

3.2.2 HIP/RPL29-deficiency induces changes in the relative distribution of bone organic and inorganic phases

The mineral-to-matrix ratio, an indicator of the relative amount of mineral to bone matrix, was analyzed in the trabecular and cortical bone of maturing and adult bone using FTIR and results were reported previously (Sloofman et al., 2010) and summarized in Figure 11. We found a significant increase in the mineral-to-matrix ratio in 6 month-old mature trabecular adult bone compared with age-matched WT controls [Figure 11, +20.2% in null (n=8) vs. WT (n=9); p =0.02]. A significant increase of 23% was also observed in the mineral-to-matrix ratio in null trabecular bone from 1 to 6 months (p=0.02). Note that this parameter only significantly increased in WT cortical bone as animals matured, as shown in Figure 11; null (n=10) vs. WT (n-10); p=0.025]. This lowered mineral-to-matrix ratio showed a highly significant 30% increase from 1 to 6 months in mutant samples ($p<0.001$). WT samples only exhibited a 12.5% increase in this parameter over the same time interval ($p<0.01$). Genotype-dependent differences were not observed in the mineral-to-matrix ratios of three month-old cortical or trabecular bone ($n \geq 10$) (Sloofman et al., 2010).

It should be noted that the above mineral-to-matrix testing only tests the relative mineral-to-matrix concentration at the microscale level. To assess whether or not increases in the mineral phase of adult null bones were detectable at the molecular level, we analyzed the collagen content of HIP/RPL29-deficient and WT femurs. Significant changes were neither found in the quantity (per dry weight of bone) nor in the relative amount of collagen (% per total protein) in mutant bone (data not shown) versus controls. Additionally, no genotype-linked difference was noted in the specific

amino acid residues of HIP/RPL29-deficient cartilage with respect to controls (data not shown). Interestingly, despite the normal proline to hydroxyproline ratio in HIP/RPL29-null femurs, the lysine/hydroxylysine ratio noticeably increased when compared to WT controls (lys/hyl=2.9 in WT; lys/hyl=4.4 in mutants). This is indicative of a shift from hydroxylysine to non-modified lysine residues in HIP/RPL29-deficient bone (data not shown, Sloofman et al., 2010).

The increases in the mineral-to-matrix ratio during the developmental period are also coupled with a reduction in the XLR parameter, indicative of collagen maturity, in HIP/RPL29-deficient bone at 3 months (n=11) in cortical and trabecular regions compared with WT controls (n=10) by approximately 10% and 11%, respectively (Figure 12; $p<0.05$). It should be noted that the decrease in the XLR parameter was more pronounced in null female trabecular bone versus null male trabecular bone and was diminished by nearly 15% when compared with age-matched WT female littermates ($p<0.05$,data not shown). When the mice reached adulthood, the decrease in XLR evident in 3 month-old null samples was overcome (Figure 11A, D). In fact, the overall increase in the XLR parameter in null cortical bone was statistically significant (+17% from 1 month vs. 6 months) and more pronounced than the increase in control bones (Sloofman et al., 2010).

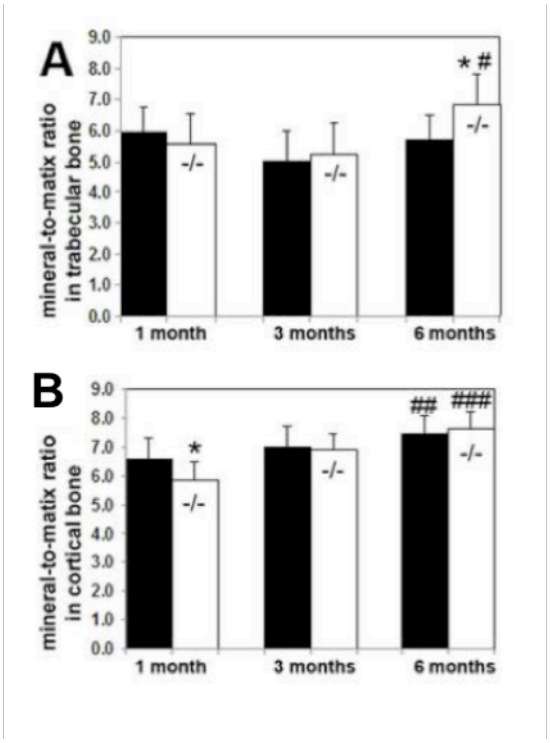

Figure 11: FTIR microspectroscopic analysis of the bone mineral-to-matrix ratio of HIP/RPL29-null and age-matched WT mice. Mean values obtained from at least eight animals per genotype for the area of phosphate band and the area of amide I band at sites below the growth plate and at mid-shaft for trabecular and cortical bone, respectively (A, D). The mineral-to-matrix ratio (*v1,v3* PO_4 area /amide I area) is below average in maturing HIP/RPL29-deficient bone when compared with WT. however, this ratio increases in older bone, with statistical significance in adult 6 month-old trabecular bones (+20.2% in nulls, n = 8 vs. WT, n = 9; *$p < 0.05$). Representative spectral infrared images of 6 month-old trabecular (B, C) and cortical bone (E, F) are shown for control and mutant samples. For mean value comparison in the same genotype in 6 months ($n \geq 8$) versus 1 month ($n \geq 10$), the p values are as follows: # $p < 0.05$, ## $p < 0.01$, ### $p < 0.001$. Adapted from Sloofman et al., 2010.

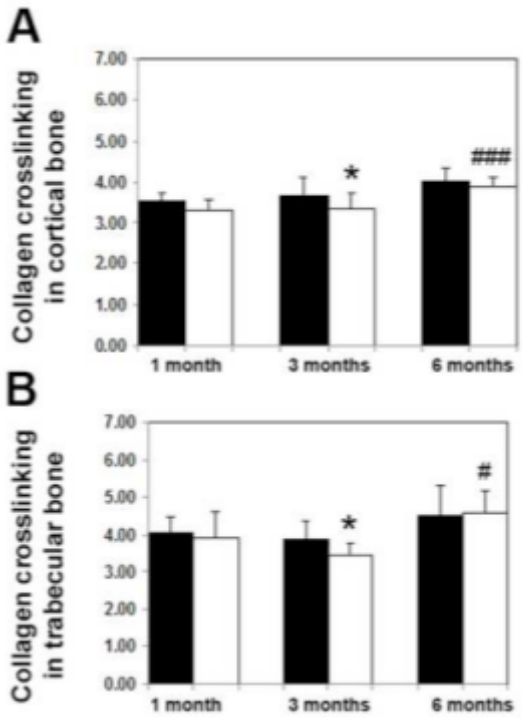

Figure 12: **FTIR analysis of the collagen crosslinking parameter in HIP/RPL29-null and age-matched WT bones.** The mean values obtained from at least eight animals in cortical (A) and trabecular bone (B) for collagen crosslinking (intensity ratio 1660/1690) are significantly reduced in HIP/RPL29-deficient bone (n=11) at 3 months (*$p < 0.05$) compared with WT (n=10) but restored to control levels in older bones. Significant increase in collagen crosslinking is seen in older null animals compared one-month-old null samples (# $p < 0.05$ and ### $p < 0.001$ in 6 months vs. 1 month, n=10). Adapted from Sloofman et al., 2010.

The carbonate-to-mineral ratio, a value that is expected to increase with age, was also examined. This ratio is related to mineral solubility. The carbonate-to-mineral ratio was slightly elevated in the trabeculae and cortices of maturing HIP/RPL29-deficient animals, however, significant changes were not observed between mutants and controls in adult bone ($n \geq 10$, data not shown, Sloofman et al., 2010). Significant changes were not observed in the size and perfection of

hydroxyapatite crystals in mutant bone tissue as evident by relatively small changes in the crystallinity parameter over time and when compared with WT controls ($n \geq 10$, data not shown, Sloofman et al., 2010). Excluding the notable decrease in the XLR parameter in female trabecular bone, significant gender-dependent differences were not found in null bones when compared with WT controls for all examined parameters (Sloofman et al., 2010).

3.2.3 HIP/RPL29-deficient first molars exhibit increases in mineral density

Micro-CT of 3 month-old HIP/RPL29-deficient (n=12) and WT (n=10) first molars, described in Table 4 revealed significant decreases of root volume (-11.3%, $p \leq 0.001$) and total volume (-7.6%, $p \leq 0.01$). Significant changes were not observed in the dentin and enamel volume were not observed, however, small but significant increases in the dentin mineral density (+2.1%, $p \leq 0.001$) and enamel mineral density (1.6%,$p \leq 0.01$) were found.

While significant gender-dependent differences in the structural properties of the first molar were not observed, differences relative to gender-matched WT samples were more pronounced in female HIP/RPL29-deficient second molars (data not shown). To gain insight behind the cause of this discrepancy, further analysis of tooth molecular composition was performed by Fourier transform microspectroscopy on female teeth (Sloofman et al., 2010).

Table 4: First molars exhibit changes in structure and mineral densities

	Controls (WT)	*HIP/RPL29-null*	
First Molar			
Total volume (mm3)	1.18 (+/- 0.05)	1.09 (+/- 9.97)	-7.6%**
Crown volume (mm3)	0.47 (+/- 0.02)	0.47 (+/- 0.04)	No change
Root volume (mm3)	0.71 (+/- 0.04)	0.63 (+/- 0.06)	-11.3%***
Dentin volume (mm3)	0.32 (+/- 0.01)	0.31 (+/- 0.03)	No change
Enamel volume (mm3)	0.12 (+/- 0.01)	0.12 (+/- 0.01)	No change
Dentin mineral density (mg/cc)	1268 (+/- 15)	1295 (+/- 17)	2.1%***
Enamel mineral density (mg/cc)	1910 (+/- 26)	1940 (+/- 27)	1.6%**

*$p<0.05$, **$p\leq0.01$, ***$p\leq0.001$; Hip/Rpl29-null (n=12) and controls (n=10). Data are mean +/- SD. Adapted from Sloofman et al, 2010

3.3 Cortical stiffness can be approximated without directly examining bone macrostructure

Having examined both the structural and molecular components of bone and teeth, we realized that the altered structure of HIP/RPL29 mutant bone resulting from HIP/RPL29 knockout could also alter cortical bone microstructure. Results from simulated three-point-bending tests show that bone geometry does not need to be directly accounted for during stiffness calculations. Both control and mutant cortical bones were simulated as 4.5-mm beams differing only in their EI measurements. In future iterations, beams were attached to the left and right side of the 4.5-mm cortical midshaft which were meant to mimic the distal and proximal ends as shown in Figure 5.

By altering the placement of the impulse (force) on each single beam, thereby accounting for experimental error, we successfully calculated reasonable stiffness measurements for hypothetical control and null bone. Results are depicted in Figure 13. Note that the parameter x_0 is the location of the applied impulse on the horizontal beam. In the first iteration, the length of the distal and proximal ends were set to zero thereby removing any direct macrostructural influences from the model.

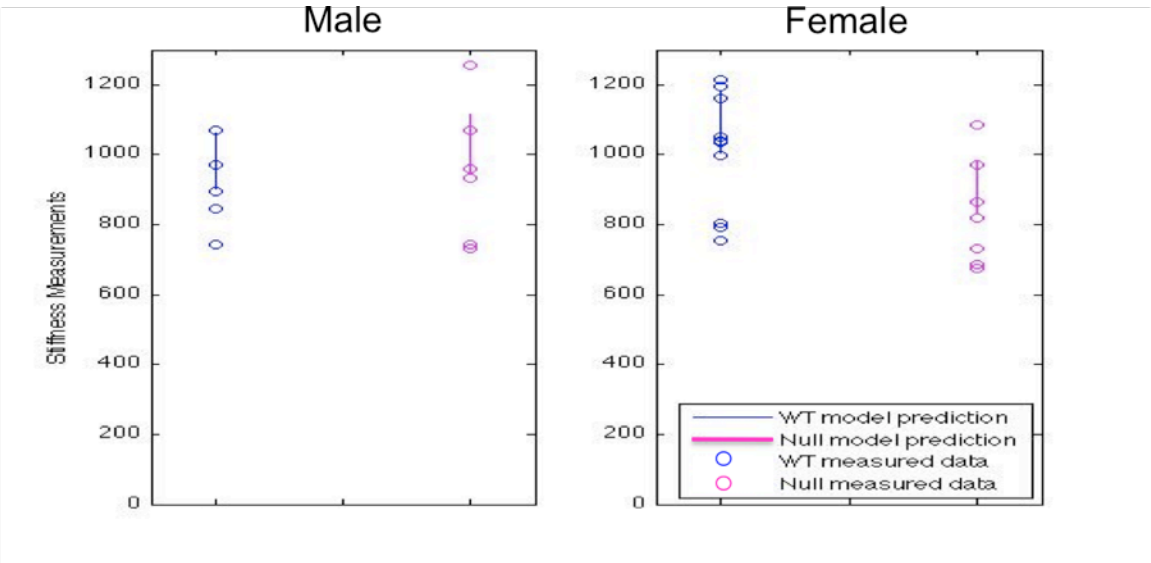

Figure 13: Femoral stiffness can be predicted without directly accounting for macroscopic structure. By varying the initial position of the impulse function, we were able to approximate a wide range of stiffness values without directly accounting for any macrostructure changes in the distal or proximal ends in 6 month-old HIP/RPL29-deficient femurs. Results for male samples are presented on the left (A) and results for female samples are presented on the right (B). Solid lines represent the stiffness prediction of the mathematical model. Circles indicate actual stiffness values obtained through biomechanical testing.

3.4 Accounting for femoral geometry decreases model accuracy

Adding the distal and the proximal ends into our mathematical model using our methodology decreased the overall accuracy of our model. In fact, the stiffness calculations for male and female control and null samples were all over-approximations, as shown in Figure 14.

Unlike our stiffness predictions in model 1 which appeared parabolic with respect to changes in position, these predictions appear cubic. This change in shape is due to the addition of the correction term described above.

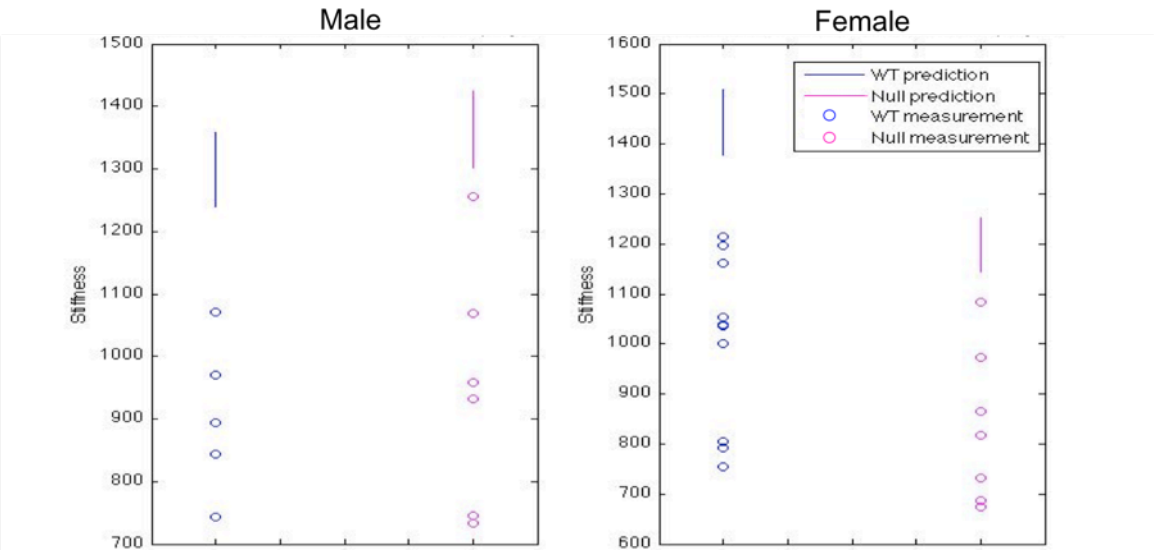

Figure 14: Introducing distal and proximal ends introduces error in stiffness calculations. Predictions of both HIP/RPL29-null and control stiffness do not fall within the range of accepted values. Results for male samples are presented on the left (A) and results for female samples are presented on the right (B). Solid lines represent the stiffness prediction of the mathematical model. Circles indicate actual stiffness values obtained through biomechanical testing.

Chapter 4

DISCUSSION

It is well established that HIP/RPL29-deficient mice exhibit a short stature phenotype resulting from embryonic development. Therefore, it was expected that significant changes in both cortical bone micro and macrostructure result from ribosomal insufficiency in the absence of HIP/RPL29.

4.1 Hip/Rpl29 knockout induces structural and material changes in bone structure and composition

Our initial studies of bone structural properties on the micro level involved analyzing adult cortical and trabecular bone using micro-CT. Both male and female femora exhibited significant decreases in size and wet weight. However, upon closer examination, the cortical bone width of HIP/RPL29-null male mice was not significantly different from controls. The preservation of cortical thickness was not evident in female samples. At 6 months, wild type bone exhibits gender specific phenotypes and male bone is generally considered more robust with a better adaption capabilities than female bones (Tommasini et al., 2007), so it is not surprising that the null phenotypes differ for both genders. In addition, only females exhibited decreases in the bone mineral density below the growth plate suggesting a higher bone turnover when compared to gender and age-matched controls.

Despite differences in structure and composition, bones in both genders failed under lower loads when compared to controls during biomechanical testing

(Oristian et al., 2009). A reciprocal relationship between geometry and material stiffness was previously documented (Jepsen et al., 2001). A significant gender difference was also seen in the elastic and post-yield phases of deformation for null bones. Male HIP/RPL29-deficient bones compensated for their inherent ribosomal insufficiency by maintaining normal bending rigidity and stiffness during elastic deformation. Female samples exhibited significant decreases in bending rigidity and stiffness when compared to controls (Oristian et al., 2009).

The most unexpected observation was the significant increase in the elastic modulus in male and female HIP/RPL29 deficient bones. The higher elasticity measurements are due to their decreased moment of inertia in the medial lateral plane. In null male samples the increased toughness compensated for the decrease in bone size which restored overall stiffness to control levels (Oristian et al., 2009). These observations are in agreement with the increased cortical BMD observed in male null samples. Decreased geometric properties have been compensated by elevating material properties in other mutant mouse models of molecules involved in endochondral bone growth (Akhter et al., 2004 and Maloul et al., 2006), so this observation is not unique to HIP/RPL29-deficient mice. However the physical consequences of the increased mineralization in bone are increased brittleness (Jepsen et al., 2001). In contrast, female HIP/RPL29-null femora were still not able to fully compensate and remained weak relative to control despite their increasing elastic properties (Oristian et al., 2009).

It has been shown that genetic mutations that alter bone architecture and tissue composition during growth can impair adult bone quality (Jepsen et al., 2007). This provides a reasonable explanation behind the altered bone growth patterns, bone

strength and fragility of HIP/RPL29-deficient mice femora. Examination of bone precursor cells *ex-vivo* also demonstrated that ribosomal insufficiency takes place in *Hip/Rpl29*-deficient cells. Since lower amounts of rRNA are present in mutant cells, less rRNA is engaged in the translationally active ribosome. We believe that ribosomal insufficiency in HIP/RPL29-null developing bone tissues may induce changes in morphological features in bone formation capacity, leading to decreased bone quality in adult mice (Sloofman et al., 2010).

Because the underlying mechanism behind the changes in the material properties in null femora is still unclear, we decided to gain insight behind the molecular composition of HIP/RPL29 bone through microspectroscopy.

4.2 Ribosomal insufficiency induces subtle organic matrix deficiencies that elevate calcification

Through FTIR, we defined the relative distribution of the organic and inorganic phases by determining the mineral-to-matrix ratios, collagen crosslinking, crystallinity and the carbonate to mineral ratio for cortical and trabecular bone and for the growth plate region. The choice of using this method was made because bone strength and stiffness, which are altered in HIP/RPL29-deficient mice, are closely correlated to mineralization, collagen density, fiber orientation and cross-linking (Martin et al., 1993). We hypothesized that differences in the relative distribution of the organic and inorganic phases, rather than the absolute quantity of mineral, were responsible for the increase in material properties in HIP/RPL29-null females (Oristian et al., 2009). It should also be noted that the elastic modulus could also be affected by changes in mineral size and shape (Boskey et al., 2006, Camacho et al.,

1999), which could have been disrupted by the alterations in translation caused by HIP/RPL29 knockout. We found that HIP/RPL29-knockout was associated with significant increases in the relative mineral content over time. However, this increase in mineralization is not correlated with changes in the global collagen content. Generally speaking, increased mineralization in bone tissue increases its brittleness and raises its fracture risk (Sloofman et al., 2010). The observed increases in the mineral-to-matrix ratio in HIP/RPL29-null samples may explain their fragility (Oristian et al., 2009).

To determine the consistency of the hypermineralization trend in HIP/RPL29-deficient mineralized tissue, we examined the composition of HIP/RPL29 null teeth and compared them to age-matched controls. Upon examination of three-month-old control and mutant molars, it was clear that structural and compositional changes were consistent with the bone phenotype. The decreases in the geometric data are consistent with the decreases in bone size. Also, two out of 12 first molar roots examined exhibited the club shape hypercementosis phenotype which is indicative of an increase in cementum deposition and the presence of abnormal mineralization foci (Pinherio et al., 2008). This phenotype agrees with the phenotype found in HIP/RPL29-deficient bone. Significant increases in dentin, and to a lesser extent enamel, density in null first molars are present relative to age-matched controls. As in bone, HIP/RPL29-deficient teeth may show an increased risk of microfracture and fragility in relation to aging. Other groups have reported increased hardness and dentin fragility in mice with mutations in either the major structural protein present in dentin (type I collagen) or in non-collagenous protein like DMP-1 (Ling et al., 2005).

To determine whether or not altered molecular composition of mutant dynamic tissue affected bone's ability to respond to mechanical stimuli, we performed cyclic mechanical loading experiments on mouse tibiae.

4.3 Bone anabolic response to load cannot be measured with extremely low mechanical load

Our results from the cyclic mechanical loading were inconclusive. We intended to load all tibiae at a frequency of 1 Hz (1 loading cycle per second). Instead we ended up loading 1 cycle every 4 seconds. To compensate for this loss, we inserted a 5 second rest period in between cycles which has been shown to stimulate bone growth in 32 week-old C3H/HeJ mice (Poliachik et al., 2008). In other words, we ended up loading the tibiae in live mice 25% slower than in established loading protocols. Our main objective was to use the Instron machine to simulate the impact of human walking on mice. Instead, our modified protocol simulated slow walking and did not allow detection of measurable changes between loaded and non-loaded control tibiae. While results from this protocol might have been applicable to disabled or elderly individuals, any outcome from this study would have minimal impact for the general population.

Altogether, these results along with results from FTIR, led us to examine the effect of decreased loading and bone geometry during growth on adult HIP/RPL29-null adult bone properties. Since HIP/RPL29-null mouse bone growth and development is likely to be affected by altered mechanical load, we hypothesized that the reduced load on HIP/RPL29-null tibiae caused by the reduced length and mass of the whole mouse and mouse skeleton could have an effect on the cortical bone

microstructure. By simulating a hypothetical femur using the beam theory, we estimated the effect of bone geometry on stiffness calculations in the HIP/RPL29-null bone.

4.4 Utilizing beam theory to calculate stiffness in HIP/RPL29-deficient femurs is appropriate

It has been shown that the structure of bone influences its ability to tolerate mechanical load. Likewise, bone adapts to loading by altering its material composition through successive modeling and remodeling (Seeman et al., 2008). Therefore, it is possible that certain changes in bone microstructure directly stem from the decrease in load in HIP/RPL29-null mice, and from the decrease in mouse and hindlimb size. While the demonstrated changes in bone microstructure directly resulting from the deletion of HIP/RPL29 are highly non-trivial (Sloofman et al., 2010), the possible indirect alterations in bone composition resulting from HIP/RPL29 knockout should not be ignored.

With the exception of extreme outliers, the first iteration of this model was able to give reasonable stiffness approximations. However, this first model did not directly account for femoral geometry and two inherent flaws of this approach are as follows:

1. EI was found using the three-point-bending test so any deviation in HIP/RPL29-null samples could be explained by the micro and the macrostructural changes in the bone.
2. EI and stiffness can vary widely, even in small sections of cortical bone so this model, along with the three-point bending test results, has limited applicability outside this experiment.

Furthermore, EI measurement is fully dependent on bone geometry. Therefore, it is impossible to accurately estimate the contribution of bone geometry to stiffness measurements. However, this mathematical model provides evidence that femoral geometry does not need to be directly accounted for during stiffness calculations using beam theory since our first model yielded accurate results.

4.5 Conclusions

A summary of discoveries and future work are presented in Figure 15. It has been established that HIP/RPL29-deficient bone exhibits both a short stature phenotype and a brittle bone phenotype. Since HIP/RPL29-deficient mice are subject to decreased mechanical loading due to their altered physical characteristics, it is possible that alterations in bone microstructural properties in HIP/RPL29-null bone are directly altered by *Hip/Rpl29* gene knockout and indirectly changed as a result from ribosomal insufficiency and subsequent loading decrease.

From the present studies, we know that delayed bone growth and overall reduction in structural properties are coupled with increased material property and elasticity in mutant samples. In addition, subtle alterations in the organic and inorganic phases of mutant bone microstructure are observed. For instance, a decrease in the collagen crosslinking parameter along with an increase in the mineral-to-matrix ratio in null samples with respect to controls results in mutant bone with lowered quality. Unfortunately, the direct impact of the short stature phenotype on any of these measurements cannot be measured.

Nonetheless, we can make limited conclusions about the impact of the short stature phenotype on stiffness measurements, given the preliminary results from

our mathematical modeling. It does not appear that sample length has to be accounted for when taking stiffness measurements. Since increasing the bone geometry complexity resulted in inaccurate results, it is clear that more work needs to be done to improve this model to increase its biological accuracy.

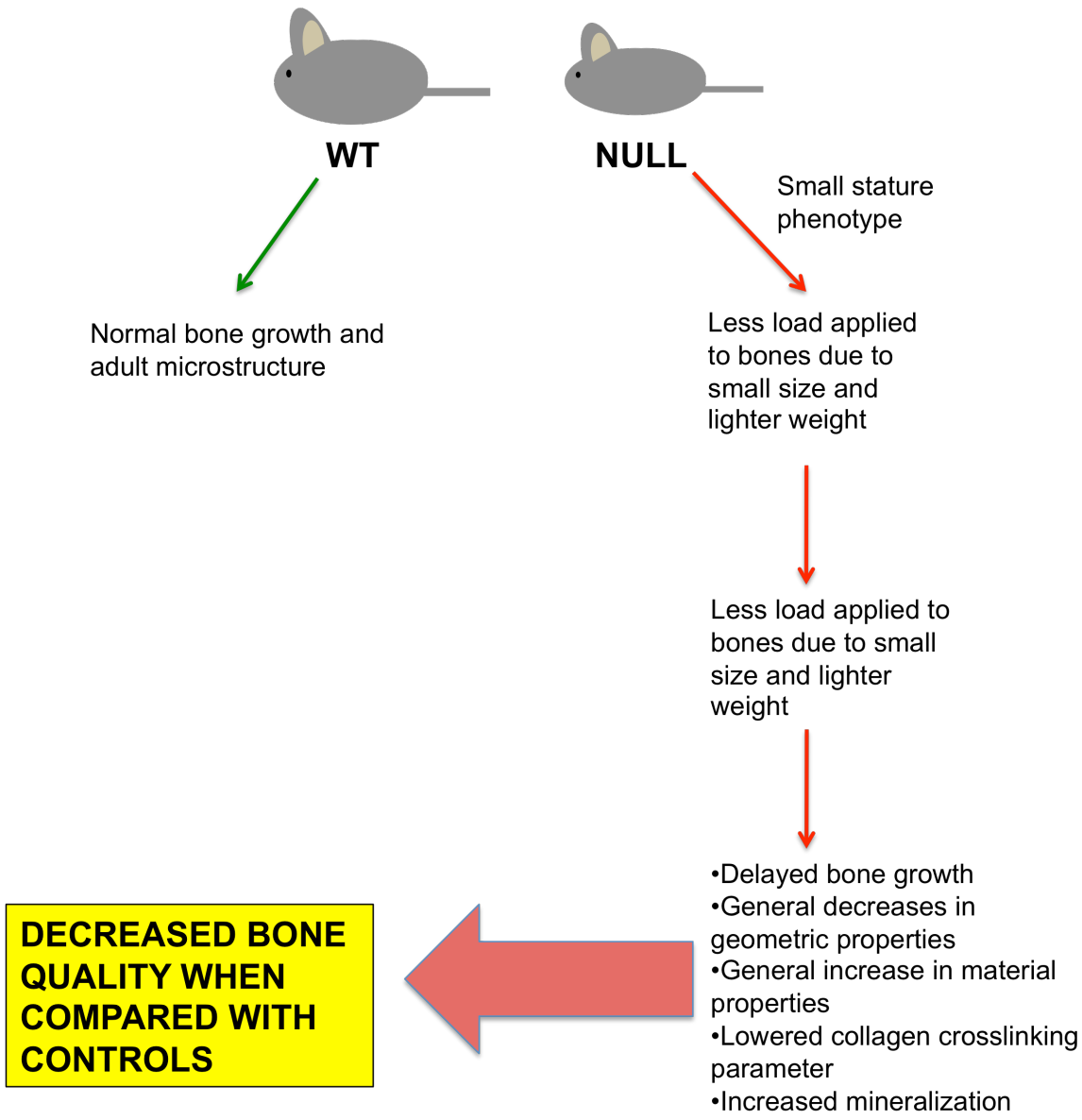

Figure 15: Summary describing impact of HIP/RPL29 knockout on bone composition. The small stature phenotype, along with inherent changes on the molecular level due to the absence of this ribosomal protein, are directly responsible for the decreased bone quality of HIP/RPL29-deficient samples when compared with controls.

REFERENCES

Akhter, M. P., D. J. Wells, S. J. Short, D. M. Cullen, M. L. Johnson, G. R. Haynatzki, P. Babij, et al. 2004. Bone biomechanical properties in LRP5 mutant mice. *Bone* 35, (1) (Jul): 162-9.

Boskey, A. L. 2006. Assessment of bone mineral and matrix using backscatter electron imaging and FTIR imaging. *Current Osteoporosis Reports* 4, (2) (Jun): 71-5.

Brodersen, D. E., and P. Nissen. 2005. The social life of ribosomal proteins. *The FEBS Journal* 272, (9) (May): 2098-108.

Camacho, N. P., S. Rinnerthaler, E. P. Paschalis, R. Mendelsohn, A. L. Boskey, and P. Fratzl. 1999. Complementary information on bone ultrastructure from scanning small angle X-ray scattering and fourier-transform infrared microspectroscopy. *Bone* 25, (3) (Sep): 287-93.

Capel, M. S., and V. Ramakrishnan. 1988. Neutron-scattering topography of proteins of the small ribosomal subunit. *Methods in Enzymology* 164, : 117-31.

Cowin, S. C. 1995. On the minimization and maximization of the strain energy density in cortical bone tissue. *Journal of Biomechanics* 28, (4) (4): 445-7.

Hoke, D. E., E. G. Regisford, J. Julian, A. Amin, C. Begue-Kirn, and D. D. Carson. 1998. Murine HIP/L29 is a heparin-binding protein with a restricted pattern of expression in adult tissues. *The Journal of Biological Chemistry* 273, (39) (Sep 25): 25148-57.

Jepsen, K. J., B. Hu, S. M. Tommasini, H. W. Courtland, C. Price, C. J. Terranova, and J. H. Nadeau. 2007. Genetic randomization reveals functional relationships among morphologic and tissue-quality traits that contribute to bone strength and fragility. *Mammalian Genome : Official Journal of the International Mammalian Genome Society* 18, (6-7) (Jul): 492-507.

Jepsen, K. J., D. E. Pennington, Y. L. Lee, M. Warman, and J. Nadeau. 2001. Bone brittleness varies with genetic background in A/J and C57BL/6J inbred mice. *Journal of Bone and Mineral Research : The Official Journal of the American Society for Bone and Mineral Research* 16, (10) (Oct): 1854-62.

Kirn-Safran, Catherine, Joanne Julian, Jennifer E. Fongemie, David E. Hoke, Kirk J. C. Czymmek, and Daniel D. Carson. 2002. Changes in the cytologic distribution of heparin/heparan sulfate interacting protein/ribosomal protein L29 (HIP/RPL29) during in vivo and in vitro mouse mammary epithelial cell expression and differentiation. *Developmental Dynamics* 223, (1) (01): 70-84.

Kirn-Safran, C. B., S. Dayal, P. A. Martin-DeLeon, and D. D. Carson. 2000. Cloning, expression, and chromosome mapping of the murine Hip/Rpl29 gene. *Genomics* 68, (2) (Sep 1): 210-9.

Kirn-Safran, C. B., D. S. Oristian, R. J. Focht, S. G. Parker, J. L. Vivian, and D. D. Carson. 2007. Global growth deficiencies in mice lacking the ribosomal protein HIP/RPL29. *Developmental Dynamics : An Official Publication of the American Association of Anatomists* 236, (2) (Feb): 447-60.

Koller, D. L., J. Schriefer, Q. Sun, K. L. Shultz, L. R. Donahue, C. J. Rosen, T. Foroud, W. G. Beamer, and C. H. Turner. 2003. Genetic effects for femoral biomechanics, structure, and density in C57BL/6J and C3H/HeJ inbred mouse strains. *Journal of Bone and Mineral Research : The Official Journal of the American Society for Bone and Mineral Research* 18, (10) (Oct): 1758-65.

Ling, Y., H. F. Rios, E. R. Myers, Y. Lu, J. Q. Feng, and A. L. Boskey. 2005. DMP1 depletion decreases bone mineralization in vivo: An FTIR imaging analysis. *Journal of Bone and Mineral Research : The Official Journal of the American Society for Bone and Mineral Research* 20, (12) (Dec): 2169-77.

Liu, Jian-Jun, Bao Hua Huang, Jinqiu Zhang, Daniel D. Carson, and Shing Chuan Hooi. 2006. Repression of HIP/RPL29 expression induces differentiation in colon cancer cells. *Journal of Cellular Physiology* 207, (2) (05): 287-92.

Maloul, A., K. Rossmeier, B. Mikic, V. Pogue, and T. Battaglia. 2006. Geometric and material contributions to whole bone structural behavior in GDF-7-deficient mice. *Connective Tissue Research* 47, (3): 157-62.

Martin, R. B. 2000. Toward a unifying theory of bone remodeling. *Bone* 26, (1) (1/1): 1-6.

Martin, R. B., and D. L. Boardman. 1993. The effects of collagen fiber orientation, porosity, density, and mineralization on bovine cortical bone bending properties. *Journal of Biomechanics* 26, (9) (Sep): 1047-54.

Oliver, E. R., T. L. Saunders, S. A. Tarle, and T. Glaser. 2004. Ribosomal protein L24 defect in belly spot and tail (bst), a mouse minute. *Development (Cambridge, England)* 131, (16) (Aug): 3907-20.

Oristian, D. S., L. G. Sloofman, X. Zhou, L. Wang, M. C. Farach-Carson, and C. B. Kirn-Safran. 2009. Ribosomal protein L29/HIP deficiency delays osteogenesis and increases fragility of adult bone in mice. Journal of Orthopaedic Research : Official Publication of the Orthopaedic Research Society 27, (1) (Jan): 28-35.

Oristian, D.. Skeletal phenotype of mice lacking HIP/RPL29, a component of the large ribosomal subunit. M.S. diss., University of Delaware ,2007. In Dissertations & Theses @ University of Delaware [database on-line]; available from http://www.proquest.com (publication number AAT 1446845; accessed May 17, 2010).

Pinheiro, B. C., T. N. Pinheiro, A. L. Capelozza, and A. Consolaro. 2008. A scanning electron microscopic study of hypercementosis. Journal of Applied Oral Science : Revista FOB 16, (6) (Nov-Dec): 380-4.

Poliachik, S. L., D. Threet, S. Srinivasan, and T. S. Gross. 2008. 32 wk old C3H/HeJ mice actively respond to mechanical loading. *Bone* 42, (4) (Apr): 653-9.

Robinson, R. A. 1952. An electron-microscopic study of the crystalline inorganic component of bone and its relationship to the organic matrix. *The Journal of Bone and Joint Surgery.American Volume* 34-A, (2) (Apr): 389,435; passim.

Rohde, L. H., J. Julian, A. Babaknia, and D. D. Carson. 1996. Cell surface expression of HIP, a novel heparin/heparan sulfate binding protein, of human uterine epithelial cells and cell lines. *The Journal of Biological Chemistry* 271, (20) (May 17): 11824-30.

Ruimerman, R., P. Hilbers, B. van Rietbergen, and R. Huiskes. 2005. A theoretical framework for strain-related trabecular bone maintenance and adaptation. *Journal of Biomechanics* 38, (4) (4): 931-41.

Schriefer, Jennifer L., Alexander G. Robling, Stuart J. Warden, Adam J. Fournier, James J. Mason, and Charles H. Turner. 2005. A comparison of mechanical properties derived from multiple skeletal sites in mice. *Journal of Biomechanics* 38, (3) (3): 467-75.

Seeman, E., and P. D. Delmas. 2006. Bone quality--the material and structural basis of bone strength and fragility. *The New England Journal of Medicine* 354, (21) (May 25): 2250-61.

Sloofman, Laura G., Kostas Verdelis, Lyudmila Spevak, Majd Zayzafoon, Mistuo Yamauchi, Lynn M. Opdenaker, Mary C. Farach-Carson, Adele L. Boskey, and Catherine B. Kirn-Safran. Effect of HIP/ribosomal protein L29 deficiency on mineral properties of murine bones and teeth. *Bone* In Press, Uncorrected Proof, .

Stoffler, G., and M. Stoffler-Meilicke. 1984. Immunoelectron microscopy of ribosomes. *Annual Review of Biophysics and Bioengineering* 13, : 303-30.

Tommasini, Steven M., Philip Nasser, and Karl J. Jepsen. 2007. Sexual dimorphism affects tibia size and shape but not tissue-level mechanical properties. *Bone* 40, (2) (2): 498-505.

APPENDIX

I. Author contributions for Oristian et al., 2010

RIBOSOMAL PROTEIN L29/HIP DEFICIENCY DELAYS OSTEOGENESIS AND INCREASES FRAGILITY OF ADULT BONE IN MICE

Daniel S. Oristian [a*], Laura G. Sloofman [a,b*], Xiaozhou Zhou [c], Liyun Wang [c],Mary C. Farach-Carson [a,d], Catherine B. Kirn-Safran [a]

[a] Department of Biological Sciences, University of Delaware, Newark, Delaware 19716

[b] Department of Mathematics, University of Delaware, Newark, DE 19716

[c] Department of Mechanical Engineering, University of Delaware, Newark, Delaware 19716

[d] Department of Materials Science and Engineering, University of Delaware, Newark, Delaware 19716

* authors contributed equally to study

C.K.S. designed research; L.G.S., harvested samples, performed micro-CT and 3-point bending tests, analyzed statistics; D.S.O., harvested samples, performed BrdU staining and micro-CT. L.W. and X.Z. assisted with mechanical testing; M.C.F.C. shared facilities and expertise in bone development; C.K.S. wrote manuscript.

II. Author contributions for Sloofman et al., 2010

EFFECT OF HIP/RIBOSOMAL PROTEIN L29 DEFICIENCY ON MINERAL PROPERTIES OF MURINE BONES AND TEETH

Laura G. Sloofman[a,f], Kostas Verdelis[b], Lyudmila Spevak[b], Majd Zayzafoon[c], Mistuo Yamauchi[d], Lynn M. Opdenaker [a], Mary C. Farach-Carson [a,e], Adele L. Boskey [b], Catherine B. Kirn-Safran [a]

[a] Department of Biological Sciences, University of Delaware, Newark, DE 19716, USA

[b] Mineralized Tissue Laboratory, Musculoskeletal Integrity Program, Hospital for Special Surgery, New York, NY 10021, USA

[c] Department of Pathology, University of Birmingham, Birmingham, AL 35294, USA

[d] North Carolina Oral Health Institute, School of Dentistry, University of North Carolina at Chapel Hill, Durham, NC 27709, USA

[e] Department of Biochemistry and Cell Biology, Rice University, Houston, TX 77005, USA

[f] Department of Mathematics, University of Delaware, Newark, DE 19716,USA

C.K.S. designed research; L.G.S., harvested and shipped samples, analyzed statistics from FT-IR and histology; L.S. and K.V. performed FT-IR; M.Z. performed histomorphometry; M.Y. performed bone biochemistry; L.M.O performed polysomal sucrose gradients; M.C.F.C. shared facilities and expertise in bone biology; C.K.S. wrote manuscript.

II. Author contributions for mathematical modeling

MATHEMATICAL MODELING OF HIP/RPL29-DEFICIENT BONE USING BEAM THEORY [UNPUBLISHED SIDE PROJECT]

Laura G. Sloofman[a,b], Catherine B. Kirn-Safran, John A. Pelesko[b]

[a] Department of Biological Sciences, University of Delaware, Newark, Delaware 19716

[b] Department of Mathematics, University of Delaware, Newark, DE 19716

L.G.S. and J.A.P. designed and implemented mathematical modeling; C.K.S. provided animal model for experimental data; L.G.S. designed MATLAB code.